Journal of Physics D: Applied Physics

On the ignition kernel formation and propagation: an experimental and modeling approach

OPEN ACCESS
IOP Publishing
Journal of Physics D: Applied Physics
J. Phys. D: Appl. Phys. **56** (2023) 225501 (25pp)
https://doi.org/10.1088/1361-6463/acc411

On the ignition kernel formation and propagation: an experimental and modeling approach

James Shaffer[1], Steven Luna[2], Weiye Wang[2], Fokion N Egolfopoulos[2] and Omid Askari[1,*]

[1] Department of Mechanical and Aerospace Engineering, West Virginia University, Morgantown, WV 26506, United States of America
[2] Department of Aerospace and Mechanical Engineering, University of Southern California, Los Angeles, CA 90089, United States of America

E-mail: omid.askari@mail.wvu.edu

Received 11 January 2023, revised 2 March 2023
Accepted for publication 14 March 2023
Published 4 April 2023

Abstract

The next generation of advanced combustion devices is being developed to operate under ultra-high-pressure conditions. However, under such extreme conditions, flame tends to become unstable and measurement of fundamental properties such as the laminar flame speed becomes challenging. One potential method to resolve this issue is measuring the ignition-affected region during spherically expanding flame experiments. The flame in this region is more resistant to perturbations and remains smooth due to the high stretch rates (i.e. small radii). Stable flame propagation allows for improved flame measurement, however, the experimentally observed kernel propagation is a function of both inflammation and ignition plasma. Therefore, the goal of the present study is to better understand the plasma formation and propagation during the ignition process, which would allow for reliable laminar flame speed measurements. To accomplish this goal, thermal plasma operating at high pressures is studied with emphasis on the spark energy effects on the formation of the ignition kernel. The thermal effect of the plasma is experimentally observed using a high-speed Schlieren imaging system. The energy dissipated within the plasma is measured with the use of voltage and current probes with a measurement of plasma sheath voltage drop as an input to numerical modeling. The measured kernel propagation rate is used to assess the accuracy of the model. The experiments and modeling are conducted in dry air at 1, 3, and 5 atm as well as in CH_4-N_2 mixtures at 1 atm, and kernel radius, temperature, and mass are reported. The voltage-drop (as a non-thermal loss) is measured to be approximately 330 $\pm$ 5 V (dry air at 1 atm) for glow plasma with a large dependency on pressure, gas composition, electrode surface quality, electrode geometry, electrode shape, and current density. The same loss within the arc plasma is measured to be 15 $\pm$ 5 V, however the arc phase loss which agrees with arc propagation is significantly higher ($\sim$45 V) which suggest additional unaccounted for phenomena occurring during the arc phase. With these losses, the modeling results are shown to predict the final kernel radius within 10%–20% of the observed kernel size. The difference found between the modeling and experimental results is determined to be a result of assuming that the primary loss mechanism (voltage drop across sheath

* Author to whom any correspondence should be addressed.

formation) remains constant for the duration of glow discharge. The discrepancy for arc discharge is discussed with several potential sources, however, additional studies are required to better understand how the arc formation affects the kernel propagation.

Keywords: ignition kernel, thermodynamics modeling, direct numerical simulation, high-speed schlieren imaging, voltage drop, glow & arc discharge

(Some figures may appear in colour only in the online journal)

1. Introduction

The understanding of the electrical discharge process is important for many practical and fundamental applications including combustion [1], chemical conversion [2], flame stabilization [3], health care [4], manufacturing and surface treatment [5] to name a few. For many combustion systems, the flame is initiated using an electrical discharge to ignite air-fuel mixtures. At the spark location, a plasma channel of ionized gas (a mixture of ions, electrons, radicals, and excited particles) forms. The ignition kernel then propagates, initiating chemical reactions followed by flame front propagation [6–8]. This flame front propagates from the surface of the ignition kernel [9, 10]. Moreover, for mixtures with a Lewis number (the thermal to mass diffusivities ratio) greater than one, there exists a minimum ignition radius [9, 11, 12] below which the flame can be quenched. This dependency on the kernel size makes the study of the ignition process crucial in quantifying plasma formation and propagation. A better understanding of the ignition process is also of great importance to improve fuel efficiency and reduce emissions under engine-relevant conditions [13]. However, this goal can be only achieved by a fundamental study on a well-optimized plasma (simple geometry, smooth structure) and under well-defined conditions (known pressure, temperature, gap size, electrode quality, flow motion, discharged energy). The effect of different plasma types and ignition sources on the early kernel geometry and structure has been discussed in various studies. In this context, we review two types of plasma (i.e. thermal and non-thermal) and a few common sources of ignition such as laser, spark discharge [14, 15], nanosecond discharge [16, 17], and dielectric barrier discharge (DBD).

Thermal and non-thermal plasmas have several differences, among them, the two important ones are: (i) the temperature of electrons in non-thermal plasmas is significantly higher than the thermal plasmas, which in the latter is equal to the temperature of heavy gas particles, and (ii) the main energy transfer mechanism in thermal plasmas is through thermal mechanisms (i.e. increasing the gas temperature via elastic collisions of electrons and heavy gas particles along with relevant transport mechanisms), while in non-thermal plasmas this occurs by both thermal (i.e. fast heat release via collisional quenching of electronically excited states) and kinetic mechanisms (i.e. rapid production of radicals and excited species via direct electron impact). The use of a laser-based ignition could provide a significant benefit from the removal of electrode interference on the ignition kernel. However, it produces a highly wrinkled early kernel and induces gas motion in the direction of the beam [18, 19]. The induced gas motion is not ideal because of the potentially non-symmetric shapes and complex geometry, which makes fundamental flame studies challenging. Ignition using non-thermal plasmas such as (1) nanosecond discharge can result in additional wrinkling via generating streamwise vorticity [20–22], and (2) DBD may not achieve the temperatures required for ignition or be limited by the geometry of the devices [23]. On the other hand, conventional spark ignition (similar to what occurs in automotive engines) has the potential to produce the most optimized kernel in terms of shape (i.e. spherically expanding) and structure (i.e. smooth surface) [24, 25]. However, this also depends on experimental factors such as electrode geometry and discharge waveform. Ziegler *et al* [26] showed that a relatively large breakdown gap of 2.6 mm produced unusual (non-symmetric) early kernel shapes. Kono *et al* [27] reported that a toroid shape was produced from the rapid expansion of breakdown [28]. Additionally, Bane *et al* [28] identified that the shape of the flat-tipped electrode resulted in vortices around the sharp edges of a flat-tipped electrode and consequently a non-smooth kernel. Therefore, it is required to optimize the spark ignition parameters to produce the desired kernel shape and structure.

In this work, the more conventional spark ignition system (i.e. capacitive discharge ignition [29]) is selected. This is because many of the discharge parameters, which affect the typical formation and propagation characteristics, are more easily controlled and understood. The spark ignition at high pressures ($>$1 atm) is a thermal plasma consisting of three distinct discharge regimes [23]: breakdown, glow, and arc. The breakdown discharge, which occurs on a time scale of 10 ns, is characterized by a sudden drop in high voltage ($>$1 kV) with a large rise in the current ($>$20 A). This is a Townsend discharge [30] where the high electric field across the gap causes the electrons to gain enough energy to cause nearly full ionization of the spark gap within a small channel. The power input results in a sudden expansion of the high-temperature channel to form a rectangular and eventually toroidal shape. The breakdown is considered insignificant for modeling the plasma discharge when the gap is sufficiently small ($<$0.4 mm). This is because the total energy deposited by the breakdown (and consequently the total effect on the kernel size) scales linearly with the gap size. The breakdown is of course necessary to precede and initiate the formation of the glow and arc plasmas. Glow discharge is initially assumed to be normal [26, 31]. Normal glow is characterized by a minimum constant current density through the surface of the cathode (i.e. high-voltage electrode) where properties of the plasma such as the

sheath formation are independent of the current [32]. Often glow discharge is referred to as non-thermal plasma, but this is highly dependent on the operating current [33]. In applications such as electronics manufacturing [5], glow discharge can be generated with low current resulting in non-thermal plasma. However, glow discharge at high currents under high pressures, which is relevant to the conditions of this work, becomes thermal plasma where local thermodynamic equilibrium (LTE) is a valid assumption [33, 34]. The arc discharge is characterized by a sudden increase in current density. Often, a current threshold where the transition to arc occurs is discussed [12] but this can be misleading as this threshold is heavily dependent on electrode material and surface quality [26]. Transition to arc discharge primarily depends on the temperature of the electrode [32] where a polished electrode prevents localized heating on the surface, extending the glow range to higher currents [35]. As a result, cooled electrodes are shown to maintain glow discharge up to 14 A at pressures of 13 atm in Cobine [32]. If the surface temperature increases, the glow discharge will eventually transition to the thermionic arc discharge [36]. Experimentally the transition between modes can be observed as a discontinuity in the voltage plot with arc discharge at a much lower voltage. The transition in discharge regimes can create non-ideal conditions for kernel formation and propagation, illustrating the need for experimental control over the spark discharge. Understanding how these discharge regimes convert the electrical energy to thermal energy in the surrounding gas is important for the development of new and improved models to better describe the complex interaction between ignition and combustion.

There exist several studies for modeling high-pressure spark ignition. Maly [9] performed multi-zone modeling to study the minimum ignition energy (MIE) where the radial temperature profile was calculated. Since Maly [9] worked backward from the flame to determine the minimal plasma characteristics for ignition, the research lacks the information to produce quantitative plasma propagation data. Lim *et al* [37] modeled both the breakdown expansion and the diffusive glow-arc discharge. The mass diffusion for the glow regime was expressed based on a correlation between the spark energy and kernel velocity, requiring adjustable constants to scale the results. In the current work however, it is assumed that the thermal conduction from the hot plasma channel into the surrounding gas is the main mechanism responsible for mass entrainment through the kernel boundary, providing a more physical definition of kernel propagation based on available transport properties. Kravchik *et al* [10] and Sher *et al* [38] provided detailed early spark propagation models with a primary focus on the breakdown stage. Since the primary ignition energy was assumed to arise from breakdown, no information regarding the glow and arc regimes was available in their studies. Kim and Anderson [39] presented a model that predicts kernel velocity utilizing experimental data at engine-relevant conditions. Their model assumed that the characteristic spark velocity is the ratio of the change in spark voltage to the electric field at the spark gap. This suggests that the kernel velocity is only a function of the plasma size (as opposed to the thermal expansion-diffusion effects which are a result of plasma discharge). As a result, the accuracy of the results is only relevant to engine results that are cycle averaged and turbulent, not the desired time-resolved propagation under well-defined conditions. Eisazadeh-Far *et al* [40] developed a thermodynamic model of spark kernel propagation under a constant mass assumption. This assumption did not account for the effects of thermal conduction, resulting in a kernel temperature much higher than the experimental data. Moreover, the ignition model was heavily dependent on the initial conditions, producing highly uncertain modeling results. Recently, Lu *et al* [41] developed a computational fluid dynamics model for the determination of MIE. However, the experimental plasma propagation data as well as the effect of different discharge regimes were not integrated into their modeling. This is very important as the thermal efficiency of a spark can vary greatly, sometimes randomly, with time as the discharge regime changes. Further analysis is required beyond these models to provide more accurate time-resolved propagation as well as mass entrainment for the ignition kernel in the glow and arc regimes. This will also help, although not within the scope of this current work, to better understand the transition region between plasma (i.e. electrical discharge driven) and a sustained flame (i.e. chemistry driven).

The goal of the present study is to develop quantitative modeling tools for plasma formation and propagation under glow/arc discharge regimes and thus to explore a well-defined plasma propagation in non-flammable gas mixtures (e.g. dry air and nitrogen-diluted methane) at high pressures ($\geqslant$1 atm). This is accomplished through two modeling approaches; a zero-dimensional (0D) thermodynamic model and a one-dimensional (1D) direct numerical simulation (DNS) model are used to predict the ignition kernel propagation. The modeling tools are compared to available experimental data to assess accuracy. In addition to modeling, extensive experimental study on the phenomena regarding the structure and properties of the plasma (sheath formation and losses) is presented as well as parametric study of significant electrode properties to better standardize and create repeatable experimental results.

2. Experimental setup

2.1. Optical setup

Experiments are conducted using a constant volume combustion chamber (CVCC) shown in figure 1. The CVCC has an internal volume with a diameter and height of 13.3 cm and uses polished quartz disks on either end to provide optical access to the ignition kernel. The experimental diagnostic includes a linear Toepler-type Schlieren system where the layout is schematically shown in figure 1. The light source is a red 625 nm Thorlabs led (model M625L4), which is collected with an initial lens (Lens 1) and focused through a 1 mm diameter pinhole to remove excess stray light and make the light as close to a

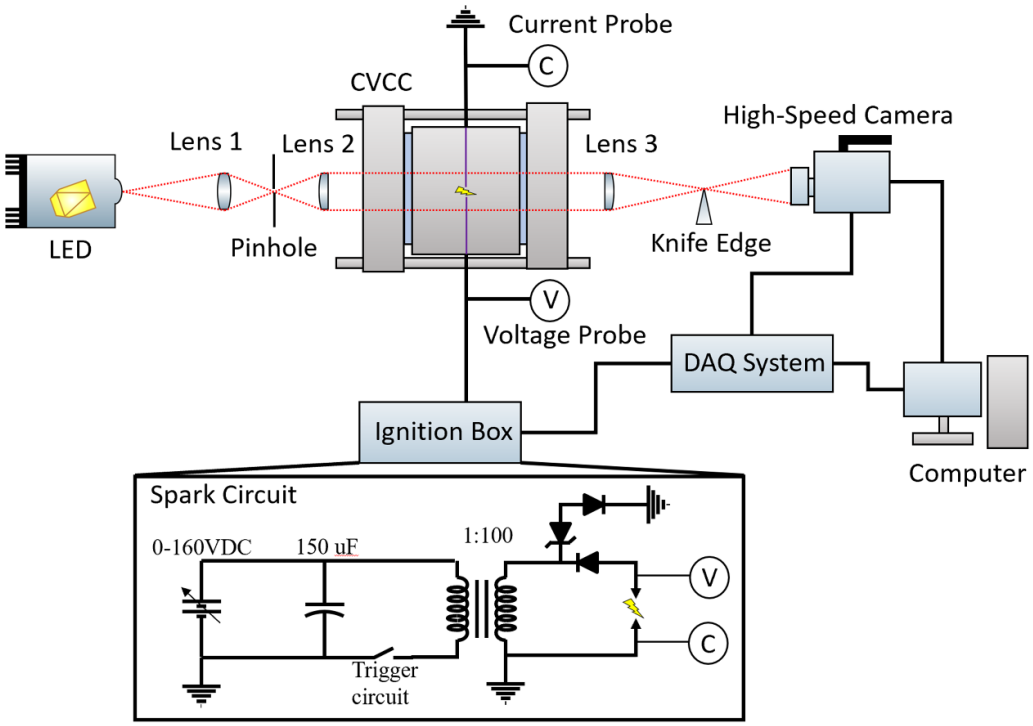

Figure 1. Schematic of the experimental configuration.

uniform point source as possible. After the pinhole, a plano-convex lens (Lens 2), with a 20 cm focal length, is used to pass collimated light through the plasma discharge, and another plano-convex lens (Lens 3), having a 40 cm focal length, for converging the light over the camera sensor. The Photron FASTCAM SA-Z high-speed camera is utilized to take images during the plasma formation (180 000 fps at 128 × 128-pixel resolution).

2.2. Electrical setup

The spark is created, at the center of CVCC, with two extended stainless steel wire electrodes [42] of 0.5 mm in diameter with tips polished to a point (conical tip) using a range of polishing methods. The spark is measured using a NorthStar PVM-4 high-voltage probe and a Pearson 6595 current coil. For kernel propagation experiments, the spark gap is held constant at 0.2 mm while this gap is changed between 0.2–4 mm for sheath measurements (see section 2.5). The spark discharge is generated by providing a high-voltage pulse to the electrodes initiated by passing a high current pulse through the primary windings of an automotive ignition coil (i.e. 5527 automotive coil). The result is a sinusoidal-like current shape driven by the second-order circuit (shown in figure 1) similar in nature to the referenced patent [43]. By changing the initially stored voltage in the capacitor, the magnitude of the glow/arc current is changed. The secondary coil sees a current pulse on the order of 1 A. The duration of the pulse is defined by the inductance and resistance of the ignition coil (∼0.7 ms for the ignition system used in the present study). The system can potentially produce multiple discharges with a single trigger event (because of underdamped oscillations); therefore, a diode system is used to suppress other discharges by passing the second discharge to the ground with an avalanche diode system.

2.3. Propagation measurement and uncertainty

Schlieren images are used to visualize kernel formation and growth. In the case of the ignition with a non-flammable mixture, the kernel propagation is driven by thermal conduction from the plasma region (for glow and arc discharge) [26, 37]. Since the largest change in density occurs near the ambient temperature, nearly the entire volume of gas heated by the plasma (i.e. ignition kernel) can be visualized by the Schlieren method [44]. The measurement of the ignition kernel involves post-processing in MATLAB to detect the kernel edge and total volume. Because the shape of observed kernels is round (no complex overlapping geometries are considered) the radius of a sphere with the equivalent volume is considered for analysis [12].

The approach to estimating the error associated with the kernel radius measurement considers three uncertainty sources including the edge location, the pixel scaling factor, and the location of the kernel center. Each of these sources is assumed to be uncertain to the size of a single pixel. The maximum and minimum radius measurement based on the variation of these parameters is calculated while processing the nominal radius size. For example, if the scaling factor is 13 px mm^{-1} then the uncertainty would include the change in kernel size if the scale were changed to 13.5 and 12.5 px mm^{-1}. Each component of uncertainty is summed in a way that the uncertainty represents the maximum potential error in the radius measurement.

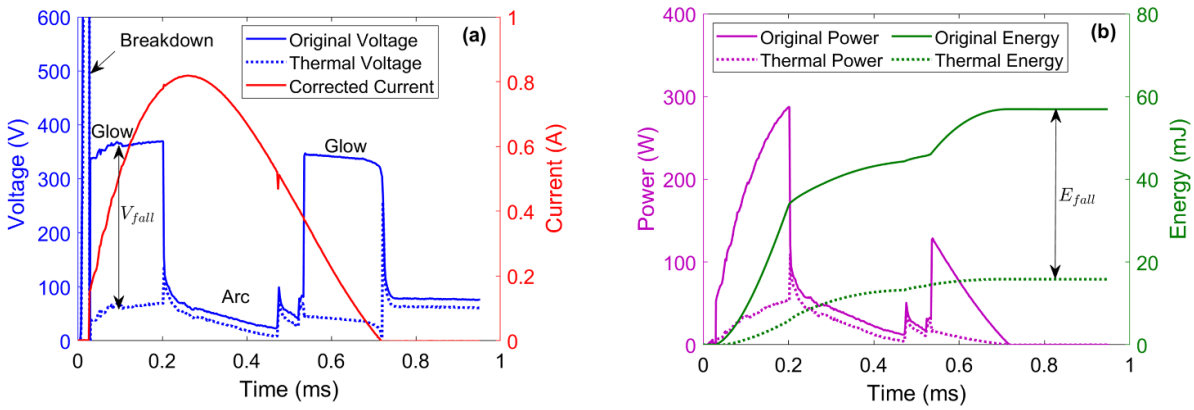

Figure 2. Typical electrical discharge characteristics across the spark gap. (a) Voltage and current waveforms and (b) power and energy waveforms.

2.4. Discharge power and uncertainty

The voltage measurement is captured using a NorthStar PVM-4 probe that has a 0.4% uncertainty, and the current is captured using a Pearson 6595 current coil which has a 1% uncertainty. The probe measurements are then captured using a NI-9222 module, four-channel analog input, with 16 bits of vertical resolution and a sample rate of 500 kHz. The inductive measurement of current is affected by signal droop which causes the actual value of current to drop over the full duration of the spark. This is corrected by using equation (1) where i_{Meas} is the signal received by the device and τ is the characteristic time constant of the current coil:

$$I = i_{\text{Meas}} + \frac{\int i_{\text{Meas}}}{\tau}. \tag{1}$$

The collected voltage and current data are used to find the discharge power as equation (2), where the V and I are the measured voltage and corrected current and $\dot{E}_{\text{elec}}$ is the total electrical spark power within the electrodes gap,

$$\dot{E}_{\text{elec}} = V(t) \times I(t). \tag{2}$$

Resistive circuit losses are excluded from this measurement through the placement of the voltage probe as close to the spark location as possible and with the use of low (<0.5 ohm) resistive electrodes. Any measured resistance between the measurement location and the ground is removed with the use of ohm's law. The thermal power $\dot{E}_{\text{th}}$ which is used as an input to the predictive models, is described in equation (3), where V_{fall} is the voltage drop across the sheath formation (see section 2.5),

$$\dot{E}_{\text{th}} = (V(t) - V_{\text{fall}}) \times I(t). \tag{3}$$

Typical discharge characteristics for voltage, current, power, and energy are shown in figure 2. The voltage waveform includes the breakdown event, which is visible as a vertical line at the start of the glow regime in figure 2(a). The glow plasma occurs for ∼0.2 ms (in this example) and at ∼350 V. Arc plasma is observed as the transition from the high voltage glow discharge to <100 V. The spark ends at ∼0.7 ms as this is the time when the current drops to 0 A. The current in this case reaches an amplitude of ∼0.8 A, which is a function of the initial capacitor energy. The power and energy of this spark event are shown for both the original and the thermal cases in figure 2(b). The thermal case, as mentioned earlier, is the case in which the voltage drop is removed, and its associated energy is released into the gas. The overall efficiency of arc plasma vs glow plasma can easily be observed in figure 2(b) where a significant ratio of glow power is lost as compared to the arc thermal/original power.

The uncertainty of the electronic measurements is determined using the total system uncertainty calculated as,

$$u_{\text{sys\_}p} = \sqrt{u_{\text{gain}}^2 + u_{\text{offset}}^2 + u_{\text{P}}^2} \tag{4}$$

where gain and offset uncertainties are 0.2% and 0.1% respectively. The u_{P} is the uncertainty associated with the probes which are 1% for the voltage probe (u_{U}) and 2% for the current probe (u_{I}). The uncertainty of the power measurement is then calculated as,

$$u_{\text{power}} = \sqrt{(I \times u_{\text{sys\_}U})^2 + (V \times u_{\text{sys\_}I})^2}. \tag{5}$$

The uncertainty of the total spark energy can additionally be propagated over time; however, this measurement is not expressly used in this analysis. Additional detail on electrical uncertainty can be found in our previous publication [45].

2.5. Sheath voltage drop measurement methodology

Since the voltage drop (often called cathode fall) can change greatly [32] with the experimental conditions (e.g. composition, geometry, pressure), it is important to measure this value. The basic voltage drop measurement method for high-pressure glow plasma employs a zero-gap extrapolation [31, 46] in which the inter-electrode distance is mechanically varied to observe the change in voltage in terms of the plasma channel length. The measurement conventionally consists of at least one flat plate electrode for the cathode such that the geometry

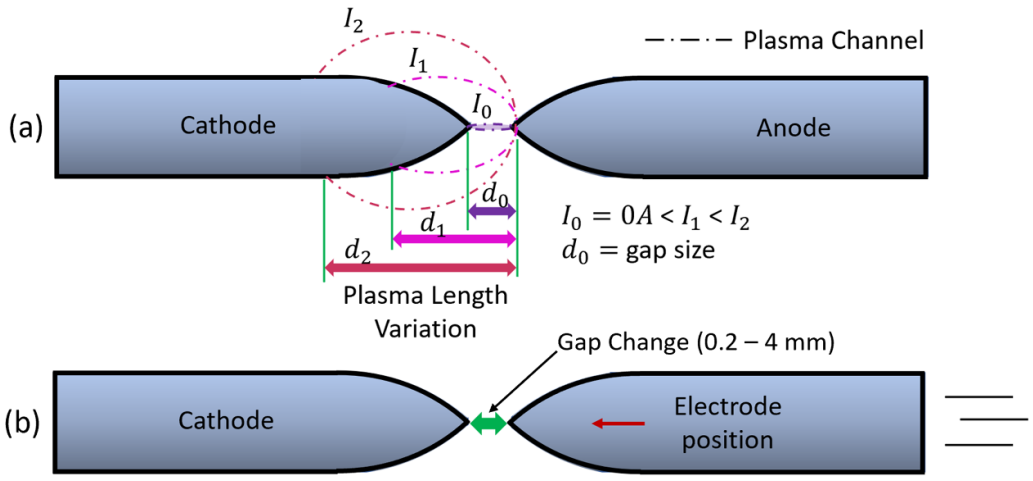

Figure 3. Illustration of plasma sheath measurement; (a) zero-current extrapolation and (b) zero-gap extrapolation.

Table 1. Summary of sheath measurement conditions.

Sheath measurements	Glow	Arc
Electrode material	Stainless steel	Stainless steel
Electrode gap size (mm)	0.2–4	0.2–4
Pressure (atm)	1–3	1–20
Surface roughness (Grit)	5000, 46 000, heavily used	5000, 46 000, heavily used
Composition	CH_4-N_2 mixture (5% CH_4 and 95% N_2) and dry air (21% O_2 and 79% N_2)	

has little effect on voltage regardless of the discharge current. In the case of the flat plate cathode, the plasma channel length is always equal to the gap distance. However, for the tip-to-tip electrode configuration, used in this paper, the plasma channel length changes with current (during the ignition process) as shown in figure 3(a).

Since the measurement of the plasma length in such a transient process using Schlieren imaging is almost impossible, it is required to have a reference case in which the plasma length can be simply obtained. The best reference case is where the plasma channel stays between the tips and its length is equal to the known value of gap size (d_0 in figure 3(a)). Although maintaining the plasma channel between the tips is experimentally challenging, it is assumed that such a condition can be satisfied when the current is very small (∼0 A). To accomplish this, an additional extrapolation (i.e. zero-current extrapolation) is required to account for the tip-to-tip electrode geometry. The zero-current extrapolation is only necessary for the glow regime as this follows a normal change in length. Therefore, the voltage drop measurement method for the tip-to-tip electrodes contains two steps. First, for each gap size, the measured voltage is plotted against the measured current. Then, the discharge voltage is extrapolated to find the zero-current voltage. Second, the zero-current voltages are plotted in terms of gap size and the voltage drop can be found by extrapolating to zero gap as seen in figure 3(b).

To assess the voltage-drop for arc discharge, the minimum voltage (when the arc is directly between the tips) is taken for several gap lengths. At least five duplicate tests are taken for each condition to ensure repeatability and assess the variability and uncertainty in the results. The estimated error of gap voltage measurements incorporates the deviation in voltage of the redundant tests at each fitting point. The final voltage drop measurement uncertainty estimates the error from the linear polynomial fit.

The effect of surface roughness, pressure, and composition on the voltage drop is also considered experimentally. Two polished levels of 5000 and 46 000 grit are considered in this work. The 5000-level grit is sandpaper while the 46 000-level grit is in the form of 0.5 μm diamond paste. In addition to surface roughness, the effect of heavy use (100+ ignition events) on the electrode is considered. The composition will naturally have a significant impact on the sheath formation and is observed for the CH_4-N_2 mixture (5% CH_4 and 95% N_2) and dry air (21% O_2 and 79% N_2). The effect of pressure on glow discharge is observed in the air up to 3 atm while the arc is observed up to 20 atm. Voltage drops for both glow and arc discharge are found utilizing different inter-electrode distances between 0.2–4 mm. Sheath measurement conditions are summarized in table 1. The measurement results and the effect of experimental conditions on voltage drop for both glow and arc will be discussed in section 4.2.

The range of data presented for the plasma sheath is selected to cover the experimental and modeling conditions. Arc sheath measurements were done up to 20 atm to support future research. For modeling purposes, various mixtures of arc and glow discharge are available from 1–5 atm making this range a suitable testbed for the proposed modeling (Note, measurement of sheath properties for glow discharge were

only possible for pressures up to 3 atm as arc interference became too large to achieve reliable glow data above this pressure).

3. Modeling approaches

A thermodynamic model and DNS model were developed for predicting the radius and temperature. The governing equations and methods are explained in the following sections. For comparative, purposes both models assume that the primary non-thermal losses arise from sheath formation at the electrodes. The net thermal energy for both models is given as,

$$\dot{E}_{\text{net}} = \dot{E}_{\text{th}} - \dot{E}_{\text{Cond}} - \dot{E}_{\text{Rad}} \tag{6}$$

where $\dot{E}_{\text{th}}$ represents the net thermal power deposited within the gas for the formation of the ignition kernel from equation (8). $\dot{E}_{\text{Cond}}$ and $\dot{E}_{\text{rad}}$ are the heat conduction [47] to the electrode and thermal radiation loss [48] from the ignition kernel, respectively below,

$$\dot{E}_{\text{Rad}} = \frac{16}{3}\pi^2 r^3 \varepsilon(T,r,p) \tag{7}$$

$$E_{\text{cond}} = \frac{\gamma}{\gamma-1} p\delta A_{\text{cond}},\ \delta = \frac{2}{\pi}\left(1-\frac{T_{\text{e}}}{T}\right)\sqrt{\alpha t} \tag{8}$$

where ε is the net emission coefficient for air [48], A_{cond} is the surface area of the electrode contacted by the kernel, γ is the specific heat ratio, T_{e} is the electrode temperature, α is the thermal diffusivity, and δ is the thermal boundary layer thickness. For the conditions observed in this work, the contribution of both conduction and radiation losses are orders of magnitude smaller than $\dot{E}_{\text{th}}$. Radiation losses only become significant at gas temperatures over 6000 K. Additionally, conduction loss may only be relevant with a significantly larger electrode [12, 49]. On the other hand, Arkhipenko *et al* [50] indicated that thermal energy conducted through the electrode is almost entirely described by sheath losses, even for a large flat plate at a steady state discharge. Despite being negligible, in the conditions presented in this work, these terms are retained to ensure the model remains relevant in other conditions such as high pressures, high currents, and large electrode geometries in future studies. Details regarding the application and scope of both models are found in the following sections.

3.1. Thermodynamic model

The thermodynamic model solves the energy and mass conservation equations to find the radius, mass, and averaged temperature of the ignition kernel. A schematic of the model is shown in figure 4 where the dashed control volume is defined as the ignition kernel edge with energy entering and exiting the system uniformly over the entire volume.

Assumptions for the thermodynamic model include: (a) unburned and burned gases behave as an ideal gas; (b) it is assumed that the kernel is approximately spherical; (c) since

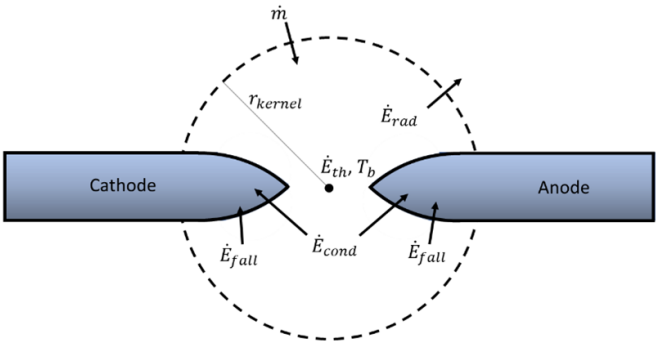

Figure 4. Schematic of the thermodynamic model for ignition kernel propagation.

the relaxation time scale of different energy modes compared to plasma expansion time is small ($\sim 10^{-9}$ s), all species are in LTE [33, 34, 38, 51, 52]; (d) the modeling begins shortly after the breakdown; (e) the only mass gain occurs from thermal conduction from the ignition kernel; (f) the radial temperature profile can be assumed linear; and (g) spark energy losses result from thermal radiation, heat conduction and sheath formation.

The model begins with energy balance,

$$m_b \frac{\mathrm{d}h_b}{\mathrm{d}t} + \frac{\mathrm{d}m_b}{\mathrm{d}t} h_b = \dot{E}_{\text{net}} + \dot{m}_i h_u \tag{9}$$

where m is the mass, h is the enthalpy, $\dot{m}$ is the mass flow rate, subscript b represents the gas heated by the plasma channel, subscript u refers to the surrounding gas, and i is the entering conditions. By solving the energy balance for the change in kernel temperature under constant pressure conditions, we find,

$$\frac{\mathrm{d}T_b}{\mathrm{d}t} = \frac{\dot{E}_{\text{net}} + \dot{m}_b(h_u - h_b)}{m_b c_{\text{p}b}} \tag{10}$$

where $\dot{m}_b = \dot{m}_i$ (the mass entering the ignition kernel) is a result of thermal conduction, T is the temperature and c_{p} is the mixture specific heat at constant pressure. This is the form of the first governing equation that can be integrated to find the average temperature of the kernel over time using the deposited thermal energy. The ideal gas equation can be used to solve for the kernel volume. All thermodynamic properties are calculated for a wide range of temperatures from Askari *et al* [53, 54]. It should be noted that the ideal gas equation can be differentiated and combined with equation (10) to directly solve for the kernel velocity shown in equation (11), where A is the kernel area and Ω is a tabulated thermodynamic property from [53, 54]. However, it is more beneficial to solve directly for the temperature:

$$\frac{\mathrm{d}r_b}{\mathrm{d}t} = \left(\frac{1}{c_{\text{p}}T_b} + \frac{\Omega}{Rc_{\text{p}}}\right) \times \frac{\dot{E}_{\text{net}}}{\rho A} + \left[\left(\frac{1}{c_{\text{p}}T_b} + \frac{\Omega}{Rc_{\text{p}}}\right)(h_u - h_b) + 1\right] \times \frac{\dot{m}_b}{\rho A}. \tag{11}$$

Thermal conduction through the gas is assumed the primary mechanism for kernel expansion. Therefore, from the energy balance perspective, the energy associated with the mass gain by the kernel propagation $\left(\dot{Q} = \dot{m}_b\left(h_b - h_u\right)\right)$ should be equal to the energy flux by thermal conduction through the Fourier heat equation which results in,

$$\dot{m}_b = \frac{Ak\frac{T_b - T_u}{1/4r}}{h_b - h_u} \tag{12}$$

where k is the thermal conductivity of air [55], r is the kernel radius, and A is the kernel area. Since the thermodynamic model is 0D, a linear temperature change is assumed across the radius. The calculated kernel temperature T_b is assumed to be the spatially averaged temperature of a spherical kernel. The radius that would correspond to the average of a linear profile would be 1/4th the radius from the kernel edge. This results in an approximate temperature gradient to use for equation (12). Equations (10) and (12), are sufficient to fully define the kernel where the kernel radius can be found using the calculated mass and temperature with the ideal gas equation. The equations are first order discretized and since the temperature is inversely proportional to the mass, a logarithmic timescale is used to ensure small initial radii can be used without temperature becoming unbounded (a result of small initial mass).

3.2. DNS model

A DNS model was developed by modifying the existing Lagrangian transient 1D reacting flow code (LTORC) [56]. The use of Lagrangian coordinates eliminates the non-linear advection term from the conservation of energy and species equations which can cause numerical instabilities [57]. The plasma is assumed to be in thermal equilibrium so that the electrons and heavy molecules are at the same temperature. Thermodynamic and chemical kinetic properties of all species are computed using Cantera [58]. Transport properties of heavy molecules are also computed via Cantera, while electrons require special treatment.

It is assumed that the electric field produced by the discharge primarily exists in the axial direction of the electrodes and that the strength of the electric field in the radial direction is negligible. A strong electric field is required to hold a net charge in the plasma, so the plasma should maintain a neutral charge in the radial direction. The absence of any significant electric field means that heavy molecules diffuse in a Fickian manner, radially. Any deviation from neutrality will produce an electric field causing charged particles to drift. The large mobility of the electron compared to the heavy molecules means electrons are most affected and will be transported to maintain charge neutrality. In effect, the diffusive flux of electrons is computed to cancel the charge flux of ions as,

$$V_e = -\frac{1}{c_e X_e}\sum_{i\neq e} c_i X_i V_i \tag{13}$$

where the subscripts e and i are respectively the electron and species i, V_i is the diffusive velocity, X_i is the mole fraction, and c_i is the charge.

The governing equations of LTORC are given as:

$$\frac{\partial r}{\partial \psi} - \frac{1}{\rho r^2} = 0 \tag{14}$$

$$\frac{\partial P}{\partial t} = 0, \frac{\partial P}{\partial \psi} = 0 \tag{15}$$

$$\rho c_p \frac{\partial T}{\partial t} - \rho\frac{\partial}{\partial \psi}\left(r^4 \rho\lambda\frac{\partial T}{\partial \psi}\right) - \frac{\partial P}{\partial t} + \sum_i \dot{\omega}_i \Delta h_{f,i} + \rho^2 r^2 \frac{\partial T}{\partial \psi}\sum_i c_{p,i} Y_i V_i + \dot{E}_{\text{net}} = 0 \tag{16}$$

$$\rho\frac{\partial Y_i}{\partial t} + \rho\frac{\partial Y_i}{\partial \psi}\left(r^2 \rho Y_i V_i\right) - \dot{\omega}_i = 0 \tag{17}$$

and the boundary conditions are given as:

$$\left(\frac{\partial T}{\partial \psi}\right)_{r=0} = 0, \left(\frac{\partial Y_i}{\partial \psi}\right)_{r=0} = 0 \tag{18}$$

$$\left(\frac{\partial T}{\partial \psi}\right)_{r=R} = 0, \left(\frac{\partial Y_i}{\partial \psi}\right)_{r=R} = 0 \tag{19}$$

where r is the spatial coordinate, ψ is the lagrangian coordinate, ρ is density, P is pressure, c_p is the specific heat at constant pressure, T is the temperature, t is the time, λ is the thermal conductivity, $\dot{\omega}_i$ is the mass production rate of species from reactions, $\Delta h_{f,i}$ is the standard heat of formation of species i, Y_i is the mass fraction of species i, and $\dot{E}_{\text{th}}$ is the net thermal energy deposited per unit volume.

The spatial distribution of the heat source term is defined in equation (20) as used by [59, 60] where r_{dis} is the radius of the discharge kernel,

$$\dot{q}_{\text{ign}} = \frac{\dot{E}_{\text{net}}(t)}{4/3\pi r_{\text{dis}}^3}\exp\left[-\pi/4\left(\frac{r}{r_{\text{dis}}}\right)^6\right]. \tag{20}$$

The thermal conductivity of the gas is approximated to be that of an air plasma for all cases. The thermal conductivity of air is computed as a function of temperature [55]. The method of lines is used to separate the spatial and temporal terms and the spatial terms are approximated using 2nd order finite differences. Equations (14)–(19) form a system of integro-differential equations, where equation (14) needs to be integrated to solve for r before the rest of the governing equations are evaluated. This system of integro-differential equations is solved using CVODE [61]. Additional details regarding LTORC can be found in [56].

A constant Lagrangian 1D spherical grid was used initially ranging from $r = 0$ to $r = 2$ cm with $N = 1000$ grid points. To resolve the plasma physics well, grid points are focused at $r = 0$. For a grid point j, the distance between j and $j + 1$ is denoted by Δr_j. The distance between the first two grid points is made to be 20 times smaller than the last two grid points which is equivalent to $\Delta r_{N-1}/\Delta r_1 = 20$. The distance

Table 2. Subset of reactions from [62].

Reaction #	*Reaction*	B	α	E_a
1	$N + N_2 \Leftrightarrow N + N + N$	$3.00 \times 10^{+22}$	−1.6	224 951.51
2	$N_2 + O \Leftrightarrow N + N + O$	$3.00 \times 10^{+22}$	−1.6	224 951.51
3	$N_2 + N_2 \Leftrightarrow N + N + N_2$	$7.00 \times 10^{+21}$	−1.6	224 951.51
4	$N_2 + O_2 \Leftrightarrow N + N + O_2$	$7.00 \times 10^{+21}$	−1.6	224 951.51
5	$N_2 + NO \Leftrightarrow N + N + NO$	$7.00 \times 10^{+21}$	−1.6	224 951.51
6	$N^+ + N_2 \Leftrightarrow N + N + N^+$	$3.00 \times 10^{+22}$	−1.6	224 951.51
7	$N_2 + O^+ \Leftrightarrow N + N + O^+$	$3.00 \times 10^{+22}$	−1.6	224 951.51
8	$N_2 + {N_2}^+ \Leftrightarrow N + N + {N_2}^+$	$7.00 \times 10^{+21}$	−1.6	224 951.51
9	$N_2 + {O_2}^+ \Leftrightarrow N + N + {O_2}^+$	$7.00 \times 10^{+21}$	−1.6	224 951.51
10	$N_2 + NO^+ \Leftrightarrow N + N + NO^+$	$7.00 \times 10^{+21}$	−1.6	224 951.51
11	$N_2 + e^- \Leftrightarrow N + N + e^-$	$1.00 \times 10^{+25}$	−1.6	224 951.51
12	$N + O_2 \Leftrightarrow N + O + O$	$1.00 \times 10^{+22}$	−1.5	118 238.65
13	$O + O_2 \Leftrightarrow O + O + O$	$1.00 \times 10^{+22}$	−1.5	118 238.65
14	$N_2 + O_2 \Leftrightarrow N_2 + O + O$	$2.00 \times 10^{+21}$	−1.5	118 238.65
15	$O_2 + O_2 \Leftrightarrow O + O + O_2$	$2.00 \times 10^{+21}$	−1.5	118 238.65
16	$NO + O_2 \Leftrightarrow NO + O + O$	$2.00 \times 10^{+21}$	−1.5	118 238.65
17	$N^+ + O_2 \Leftrightarrow N^+ + O + O$	$1.00 \times 10^{+22}$	−1.5	118 238.65
18	$O^+ + O_2 \Leftrightarrow O + O + O^+$	$1.00 \times 10^{+22}$	−1.5	118 238.65
19	${N_2}^+ + O_2 \Leftrightarrow N_2^+ + O + O$	$2.00 \times 10^{+21}$	−1.5	118 238.65
20	$O_2 + {O_2}^+ \Leftrightarrow O + O + {O_2}^+$	$2.00 \times 10^{+21}$	−1.5	118 238.65
21	$NO^+ + O_2 \Leftrightarrow NO^+ + O + O$	$2.00 \times 10^{+21}$	−1.5	118 238.65
22	$N + NO \Leftrightarrow N + N + O$	$1.10 \times 10^{+17}$	0	150 033.91
23	$NO + O \Leftrightarrow N + O + O$	$1.10 \times 10^{+17}$	0	150 033.91
24	$N_2 + NO \Leftrightarrow N + N_2 + O$	$5.00 \times 10^{+15}$	0	150 033.91
25	$NO + O_2 \Leftrightarrow N + O + O_2$	$5.00 \times 10^{+15}$	0	150 033.91
26	$NO + NO \Leftrightarrow N + NO + O$	$1.10 \times 10^{+17}$	0	150 033.91
27	$N^+ + NO \Leftrightarrow N + N^+ + O$	$1.10 \times 10^{+17}$	0	150 033.91
28	$NO + O^+ \Leftrightarrow N + O + O^+$	$1.10 \times 10^{+17}$	0	150 033.91
29	${N_2}^+ + NO \Leftrightarrow N + {N_2}^+ + O$	$5.00 \times 10^{+15}$	0	150 033.91
30	$NO + {O_2}^+ \Leftrightarrow N + O + {O_2}^+$	$5.00 \times 10^{+15}$	0	150 033.91
31	$NO + NO^+ \Leftrightarrow N + NO^+ + O$	$5.00 \times 10^{+15}$	0	150 033.91
32	$NO + O \Leftrightarrow N + O_2$	$8.40 \times 10^{+12}$	0	38 651.12
33	$N_2 + O \Leftrightarrow N + NO$	$6.40 \times 10^{+17}$	−1	76 308.64
34	$N + O \Leftrightarrow NO^+ + e^-$	$8.80 \times 10^{+08}$	1	63 391.81
35	$O + O \Leftrightarrow O_2^+ + e^-$	$7.10 \times 10^{+02}$	2.7	160 168.65
36	$N + N \Leftrightarrow N_2^+ + e^-$	$4.40 \times 10^{+07}$	1.5	134 136.28
37	$NO^+ + O \Leftrightarrow N^+ + O_2$	$1.00 \times 10^{+12}$	0.5	153 412.16
38	$N^+ + N_2 \Leftrightarrow N + {N_2}^+$	$1.00 \times 10^{+12}$	0.5	24 243.89
39	$N + {O_2}^+ \Leftrightarrow N^+ + O_2$	$8.70 \times 10^{+13}$	0.14	56 834.04
40	$NO + O^+ \Leftrightarrow N^+ + O_2$	$1.40 \times 10^{+05}$	1.9	52 859.63
41	$N_2 + {O_2}^+ \Leftrightarrow N_2^+ + O_2$	$9.90 \times 10^{+12}$	0	80 879.21
42	$O + {O_2}^+ \Leftrightarrow O^+ + O_2$	$4.00 \times 10^{+12}$	−0.09	35 769.67
43	$N + NO^+ \Leftrightarrow N_2 + O^+$	$3.40 \times 10^{+13}$	−1.08	25 436.21
44	$NO^+ + O_2 \Leftrightarrow NO + {O_2}^+$	$2.40 \times 10^{+13}$	0.41	64 782.85
45	$NO^+ + O \Leftrightarrow N + {O_2}^+$	$7.20 \times 10^{+12}$	0.29	96 578.12
46	$N_2 + O^+ \Leftrightarrow N_2^+ + O$	$9.10 \times 10^{+11}$	0.36	45 308.25
47	$N + NO^+ \Leftrightarrow N_2^+ + O$	$7.20 \times 10^{+13}$	0	70 545.75
48	$O + e^- \Leftrightarrow O^+ + e^- + e^-$	$3.90 \times 10^{+33}$	−3.78	314 971.86
49	$N + e^- \Leftrightarrow N^+ + e^- + e^-$	2.50E + 34	−3.82	335 042.62

between grid points is gradually increased with r such that $\Delta r_{j+1}/\Delta r_j = (\Delta r_{N-1}/\Delta r_1)^{\frac{1}{N-1}}$.

A mixture-averaged transport model is used to compute the diffusive velocity of heavy molecules. Two different chemical kinetic models were used, one for air and another for N_2/CH_4 mixtures. For air, a subset of reactions from the model by Park [62] was used as listed in table 2. For N_2/CH_4 mixture, the entirety of the FFCM1 model [63], a subset of the Park model [62] as listed in table 2, and a subset of the Eichwald *et al* model [64] as listed in table 3 were combined. All reaction

Table 3. Subset of reactions from [64].

Reaction #	*Reactions*	*B*	α	E_a
50	$H_2O^+ + e^- \Leftrightarrow OH + H$	3.80×10^{-07}	0	0
51	$H_2O^+ + e^- \Leftrightarrow H_2 + O$	1.40×10^{-07}	0	0
52	$H_2O^+ + e^- \Leftrightarrow H + H + O$	1.70×10^{-07}	0	0
53	$N^+ + OH \Leftrightarrow OH^+ + N$	3.40×10^{-10}	0	0
54	$N^+ + OH \Leftrightarrow NO^+ + H$	3.40×10^{-10}	0	0
55	$N^+ + H_2O \Leftrightarrow H_2O^+ + N$	2.40×10^{-09}	0	0
56	$N^+ + H_2O \Leftrightarrow NO^+ + H_2$	4.00×10^{-09}	0	0
57	$N^+ + CO \Leftrightarrow CO^+ + N$	4.90×10^{-09}	0	0
58	$N^+ + CO_2 \Leftrightarrow CO_2^+ + N$	1.30×10^{-09}	0	0
59	$N^+ + CO_2 \Leftrightarrow CO^+ + NO$	2.50×10^{-10}	0	0
60	$N_2^+ + H_2O \Leftrightarrow H_2O^+ + N_2$	2.00×10^{-09}	0	0
61	$O^+ + H_2 \Leftrightarrow OH^+ + H$	1.80×10^{-09}	0	0
62	$O^+ + OH \Leftrightarrow OH^+ + O$	3.30×10^{-10}	0	0
63	$O^+ + OH \Leftrightarrow O_2^+ + H$	3.60×10^{-10}	0	0
64	$O^+ + H_2O \Leftrightarrow H_2O^+ + O$	2.70×10^{-09}	0	0
65	$O^+ + CO_2 \Leftrightarrow O_2^+ + CO$	1.00×10^{-09}	0	0
66	$OH^+ + NO \Leftrightarrow NO^+ + OH$	4.60×10^{-10}	0	0
67	$OH^+ + H_2 \Leftrightarrow H_2O^+ + H$	1.30×10^{-09}	0	0
68	$OH^+ + OH \Leftrightarrow H_2O^+ + O$	7.00×10^{-10}	0	0
69	$OH^+ + H_2O \Leftrightarrow H_2O^+ + OH$	1.50×10^{-09}	0	0
70	$H_2O^+ + O \Leftrightarrow O_2^+ + H_2$	5.50×10^{-11}	0	0
71	$H_2O^+ + O_2 \Leftrightarrow O_2^+ + H_2O$	2.60×10^{-10}	0	0
72	$H_2O^+ + N \Leftrightarrow NO^+ + H_2$	9.00×10^{-11}	0	0
73	$H_2O^+ + NO \Leftrightarrow NO^+ + H_2O$	6.00×10^{-10}	0	0
74	$CO^+ + O \Leftrightarrow O^+ + CO$	1.40×10^{-10}	0	0
75	$CO^+ + O_2 \Leftrightarrow O_2^+ + CO$	1.00×10^{-10}	0	0
76	$CO^+ + NO \Leftrightarrow NO^+ + CO$	3.30×10^{-10}	0	0
77	$CO^+ + OH \Leftrightarrow OH^+ + CO$	2.50×10^{-10}	0	0
78	$CO^+ + OH \Leftrightarrow CO_2^+ + H$	2.10×10^{-10}	0	0
79	$CO^+ + H_2O \Leftrightarrow H_2O^+ + CO$	1.30×10^{-10}	0	0
80	$CO^+ + CO_2 \Leftrightarrow CO_2^+ + CO$	8.50×10^{-10}	0	0
81	$CO_2^+ + O \Leftrightarrow O_2^+ + CO$	1.30×10^{-10}	0	0
82	$CO_2^+ + O \Leftrightarrow O^+ + CO_2$	1.30×10^{-10}	0	0
83	$CO_2^+ + O_2 \Leftrightarrow O_2^+ + CO_2$	6.50×10^{-09}	−0.78	0
84	$CO_2^+ + NO \Leftrightarrow NO^+ + CO_2$	1.20×10^{-10}	0	0
85	$CO_2^+ + OH \Leftrightarrow OH^+ + CO_2$	3.00×10^{-10}	0	0
86	$CO_2^+ + H_2O \Leftrightarrow H_2O^+ + CO_2$	1.70×10^{-09}	0	0

rate coefficients computed from tables 2 and 3 are in Arrhenius form using equation (21):

$$k(T) = BT^{\alpha} \exp\left(-\frac{E_a}{R^o T}\right) \tag{21}$$

where $k(T)$ is the rate coefficient in $\mathrm{cm}^3\ \mathrm{mol}^{-1}$, B is a constant, α is the temperature exponent, E_a is the activation energy in $\mathrm{cal}^1\mathrm{mol}^{-1}$, and R^o is the universal gas constant. The LTORC simulations are initialized after breakdown and the subsequent emitted shockwave. The state of the plasma in the plasma kernel immediately after the breakdown is estimated using Cantera [58]. This is done by adding the breakdown energy to a small cylindrical volume of gas that is 0.2 mm in diameter and 0.2 mm tall and equilibrating it isochorically.

The significant discontinuity in pressure after breakdown forms a shockwave, which expands the plasma. The hydrodynamic module of AMRVAC [65] is used to solve the compressible Euler equations and simulate the change of pressure with time of the plasma kernel as it mechanically equilibrates. It is assumed that the primary cause of pressure change in the plasma during this expansion is due to the shockwave and that any change in pressure due to changes in the chemical state of the plasma is negligible. Starting from the state of the plasma after breakdown, a 0D reactor [58] is used to estimate how the thermochemical state of the plasma kernel changes during expansion by using the change of pressure vs time computed by AMRVAC. The conservation of energy and species equations of the 0D reactor are given as below,

$$\rho c_p \frac{\partial T}{\partial t} = \frac{\partial P}{\partial t} - \sum_i \dot{\omega}_i \Delta h_{f,i} \tag{22}$$

$$\rho \frac{\partial Y_i}{\partial t} = \dot{\omega}_i. \tag{23}$$

The radius and boundary layer thickness of the plasma kernel after the expansion is estimated from the final density profile of the AMRVAC simulation. These two values are used to interpolate between the post-shock state of the plasma and the state of the ambient gas to form the 1D initial conditions for LTORC.

4. Results and discussion

4.1. Spark morphology

Figure 5 depicts the snapshots of plasma kernel growth under different experimental conditions (i.e. gap size, surface quality, and gas mixture composition). Each letter represents a single experiment for a total of five experiments shown. Note that, for the 'prepared' electrode (polished), such as in figures 5(b), (c) and (e) where pure glow is observed, the results (shape and size) are highly repeatable. Much of the random nature of spark discharge comes from arc discharge. The mixtures are selected to be outside of the flammability limit to only study the plasma propagation by isolation from combustion chemistry. The current flows from the cathode (high-voltage electrode) to the anode (grounded electrode) forming an ionized region in the gap between the electrodes. Depending on the conditions, this ionized region (referred to as 'plasma channel' in this paper) is represented by either pure glow, pure arc, or combined glow-arc regimes. The high-temperature plasma channel heats the surrounding gas via thermal conduction, generating a so-called 'ignition kernel' that extends beyond the plasma channel.

It is important to distinguish between the plasma channel and ignition kernel as shown with purple dash-dotted and red dashed regions in figure 6, respectively. The plasma channel can be observed in some experimental conditions via the emission of bright light at the center of the ignition kernel. This bright emission is more pronounced in the absence of oxygen in the mixture as shown in figures 5(d)–(f) at $t = 255$ μs. The ignition kernel, which represents the density change between the heated region and surrounding gas, can be easily observed by Schlieren imaging. There also exists a thin layer (not visible in figure 5 because of the small thickness) at the surface of the cathode and anode with a large population of positive ions [66]. This layer, which is called the sheath, is responsible for a substantial electric field at the surface of the electrodes resulting in a large voltage drop. The energy dissipated within this sheath is not converted to thermal energy within the gas but is rather lost to the electrode [26, 50].

Among the parameters affecting the spark morphology, electrode geometry, surface quality (i.e. roughness), gas pressure, ignition circuit (i.e. current discharge profile), and gap size are of great importance. As shown in figure 5, the gap size and surface quality can have a significant influence on plasma regime and spark morphology. Gap size, in general, increases the path-length of the plasma current and as a result the total thermal energy dissipated. However, breakdown (not included in the modeling/experimental results) sees a far greater thermal efficiency and expansion which results in the toroidal geometry in figure 5(a). The energy released during the breakdown is proportional to the gap size where gaps with a smaller size ($\sim$0.2 mm) are found to minimize the breakdown effect as seen in figure 5(b). For glow and arc discharge the path of plasma is not only restricted to the gap and as a result is not linearly proportional as compared to breakdown for small gaps. For the case of unpolished electrodes in figure 5(d), the majority of the discharge occurs within the arc regime in contrast to the glow regime found in figure 5(e) with polished electrodes. The plasma is typically observed (via the voltage waveform and optically) to start with glow, transition to arc (if at all), then transition back to glow. If the initial glow phase is less than $\sim$20% of the discharge; the shape of the kernel is generally challenging to measure as apparent in figure 5(d).

Although the gas composition affects the kernel size (from changes in mixture properties and thermal efficiencies), no noticeable changes have been observed in the spark morphology (structure) as illustrated in figures 5(b), (c), and (e). The change in composition will change the characteristic discharge voltage as a result of these changed properties, however, the behavior of the kernel remains mostly the same. The kernel propagations shown in figures 5(a) and (d) are not preferred for the spherically expanding flame measurements because of the abnormal geometry. Therefore, the best practice is to adjust the gap size and surface quality to produce a more symmetric and uniform kernel shape as seen in figures 5(b), (c), and (e). This well-defined kernel morphology usually occurs in the volumetric glow discharge. However, maintaining the discharge in a pure glow regime is challenging particularly as pressure increases. Some arc discharge can retain a decent shape if arc occurs for a short duration.

The glow regime fully surrounds the cathode, unlike the arc that is highly localized. The constant current density, in a glow regime, results in a large discharge area on the cathode surface as shown in figure 5(a). The size of this area varies according to the supplied current. The formation of such discharge area results in a high electric field at the cathode surface causing the characteristic high voltages for glow plasma ($>$200 V). However, the arc regime is characterized by a sudden change in current density where the discharge area at the cathode is significantly decreased and forms a so-called discharge spot as depicted in figure 6(b). Such discharge transition, from a larger to a smaller area, results in a significant reduction in voltage ($<$100 V). The discharge spot on the cathode is in the same order of size as the anode however the location of the spot can vary widely. The ignition kernel is well defined through the schlieren method however the plasma region is only sometimes visible through intense direct radiation seen in figures 5(d) and (e).

4.2. Voltage drop

Figure 7(a) shows the effect of gas composition (dry air and N_2-CH_4), electrode surface quality (5000 and 46 000 grit), and electrode heavy utilization (100+ ignition events) on the voltage drop. In figure 7(a), the voltage versus gap distance

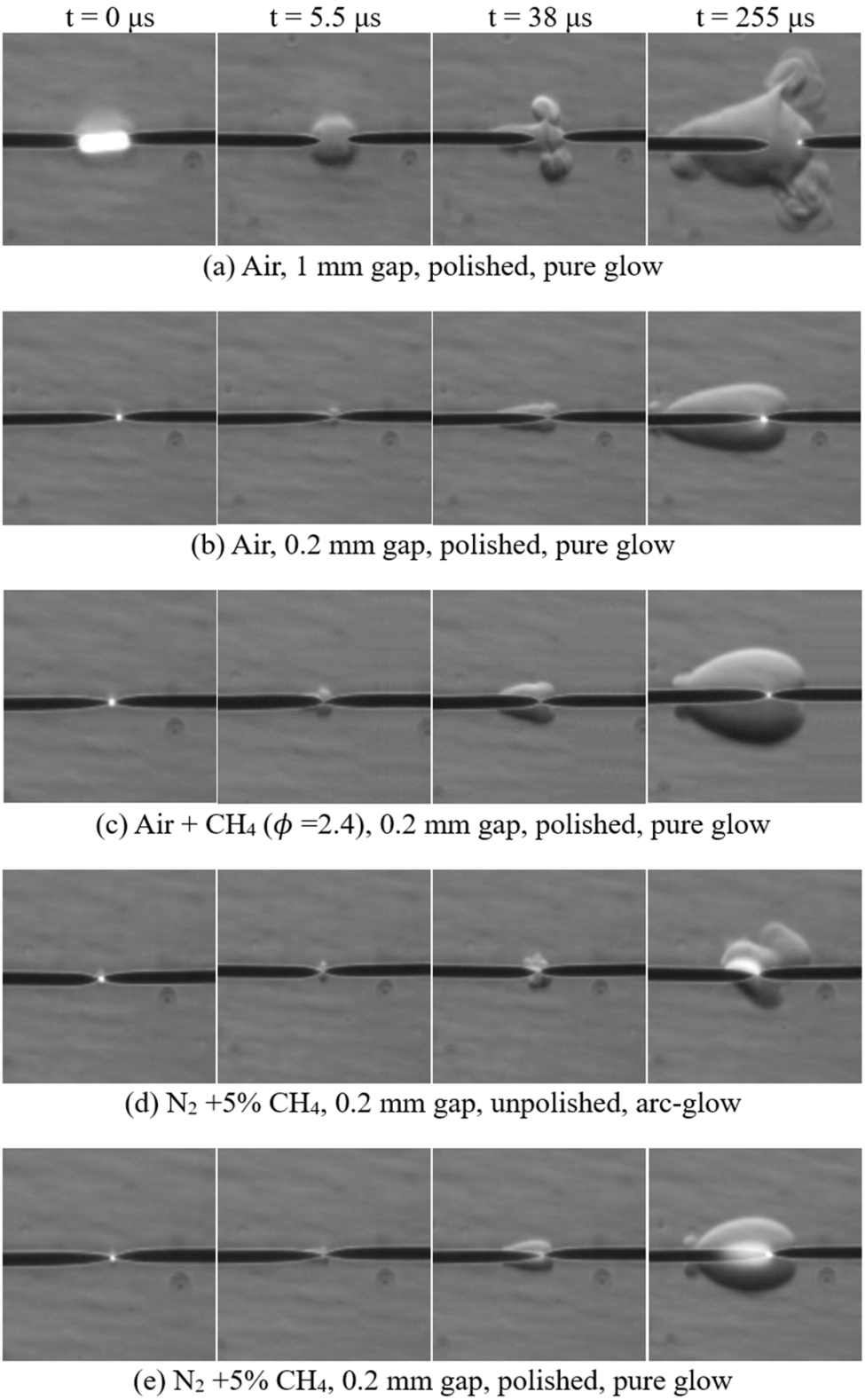

Figure 5. Snapshots of ignition kernel propagation at the pressure of 1 atm; (a) pure glow discharge in dry air (21% O_2 + 79% N_2) with polished electrodes at 1 mm gap, (b) pure glow discharge in dry air with polished electrodes at 0.2 mm gap, (c) pure glow discharge in the rich air-methane ($\phi = 2.4$) with polished electrodes at 0.2 mm gap, (d) arc-glow discharge in 95% N_2 + 5% CH_4 with unpolished electrodes at 0.2 mm gap, (e) pure glow discharge in 95% N_2 + 5% CH_4 with polished electrodes at 0.2 mm gap.

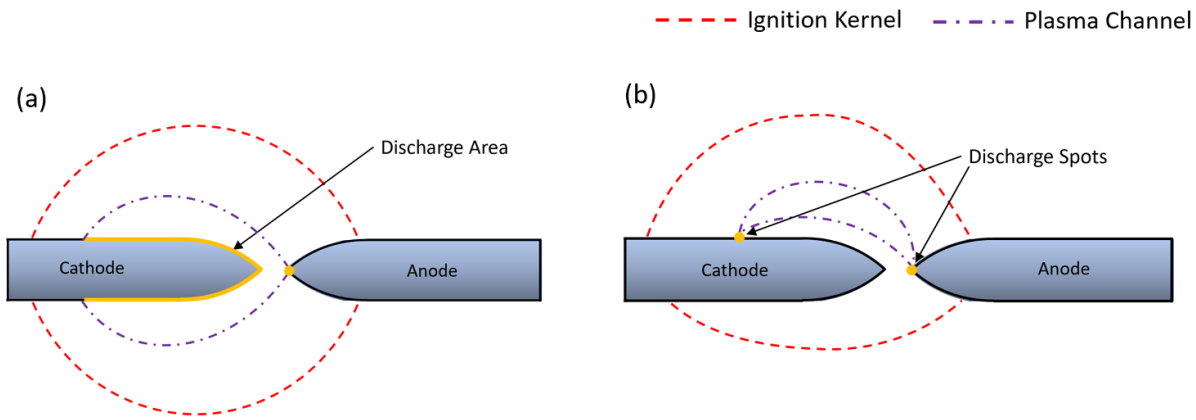

Figure 6. Illustration of (a) glow and (b) arc plasmas characteristics.

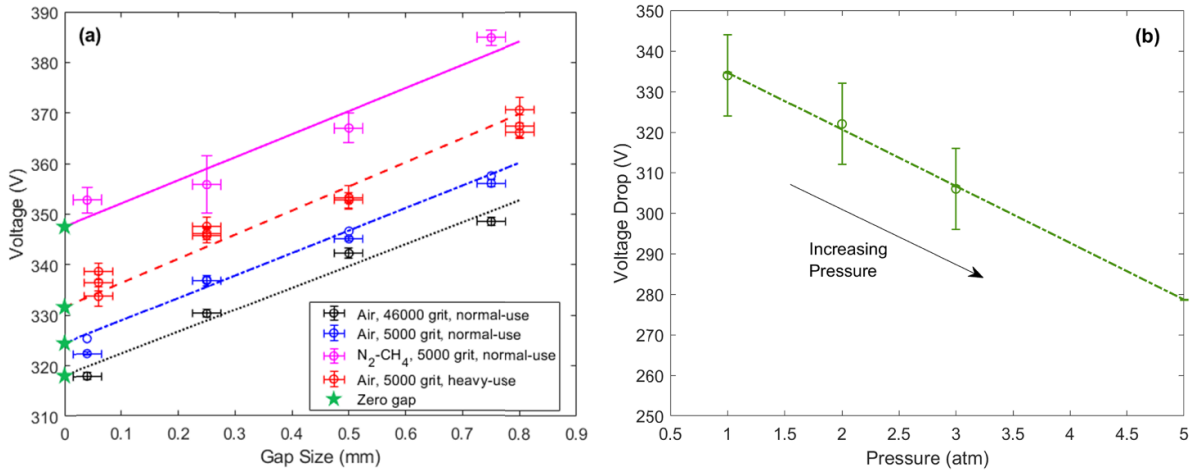

Figure 7. Effect of (a) composition, surface quality, heavy- or normal-use and (b) gas pressure on voltage drop in the glow discharge.

is shown where the circles represent the average zero-current extrapolation for a given gap. These data points are then extrapolated to the zero-gap (depicted by stars) to find the voltage drop for each experimental condition.

It is important to note that even for a small variation in experimental conditions such as the surface roughness of the electrode, there exists a significant change in the discharge characteristics. For instance, varying the electrode polish from 5000 grit (blue dash-dotted line) to 46 000 grit (black dotted line) results in a change in the overall discharge voltage by ∼5 V. The change produced by surface roughness is thought to be due to changing the work function of the material [67, 68] where the voltage drop is expected to vary linearly with the work function [32]. This change in surface conditions will affect the field emission of electrons from the electrode surface and has been accounted for in another plasma modeling such as Venkattraman [36].

Heavy electrode usage, without re-polishing/cleaning, was also observed to result in a measurable change in the voltage drop (red dashed line). Heavy-use electrode shows an increase by ∼10 V compared with the similar 5000 grit electrode under normal-use (blue dash-dotted line). This is expected to be the combined effect of the change in the electrode surface roughness and a change in electrode surface composition (formation of oxide layer). The oxide layer, discussed in the following section, results in surface deformations as well as layers that can flake from the surface (for the thickest oxide formations) [69]. This will expose larger surface areas to the plasma. Both the mechanical roughness [67, 68] and oxide composition [70] will change the electrode work function however the actual contribution of each of these effects toward the total change is beyond the scope of the work. Gas composition from dry air (blue dash-dotted line) to N_2-CH_4 (pink solid line) creates a significant increase in the sheath voltage drop of about ∼25 V. Note that, in the N_2-CH_4 case, the polish level of the electrodes is kept constant at 5000 grit.

The voltage drop reported in this work is around 330 V for stainless steel in the air. Note that heavy-use electrode in air is used for modeling as this appears to more closely represent electrode condition when the spark propagation data was recorded. Comparatively, in literature, the voltage drop reported by Cobine [32] for iron electrodes in the air (closest experimental condition) is 269 V. Swett [46] reported a 290–300 V drop for stainless steel electrodes (with cadmium) in air. It

is suggested that the differences between these reported values are a result of many factors including electrode geometry, electrode material, electrode surface quality, as well as the current magnitude. The most significant effect is likely a result of the last factor where Cobine [32] reported a normal glow discharge while the values in Swett [46] may have abnormal discharge on account of the short pulse discharge observed. The pulse observed in this work reaches much higher currents and consequently finds a much larger value. Cobine [32] also reported a wide range of pure gas compositions, which provides insight into the effect gas composition has on the sheath. When comparing discharge in air vs N_2, for copper electrodes, a significant reduction in the voltage drop, 160 V, is observed. However, discharge in a heavier molecule such as CO_2 is shown to increase the voltage drop over the air by 90 V. For the experimental condition observed in this research with O_2 removed, a reduction in the voltage drop is expected, however, just a small addition of CH_4 proves to reverse this effect.

The effect of pressure on voltage drop is shown in figure 7(b) for a heavy-use electrode. To have a sustained glow discharge, the maximum pressure is limited to 3 atm. Increasing pressure results in a decrease in the expected voltage drop since the current density at the cathode will increase as the length scale decreases (current is independent of pressure). This result shows that voltage drop is inversely proportional to the current density for the conditions observed. Additionally, increasing pressure leads to arc transition.

Sheath measurement for arc discharge over a wide range of pressures and different electrode surface roughness versus gap distance is shown in figure 8. As previously mentioned, the voltage drop corresponds to the zero-gap extrapolation (the circles in figure 8). As can be seen, no significant change in voltage drop is observed for different pressure and electrode roughness. Therefore, it is concluded that the value of voltage drop for arc discharge mode is around 15 $\pm$ 5 V and remains constant as expected since arc discharge is a result of thermionic emission [71] where the high thermal load on the material at the small discharge spot results in a more uniform condition (i.e. surface melting).

4.3. Effect of electrode surface morphology on voltage drop

The surface quality of the electrode was observed to effect the discharge characteristics of glow discharge (shown in figure 7). Qualitative understanding of this effect was explored by taking optical microscope images using a Keyence VHX-7000. The surface of the most polished electrode under normal-use (46 000 grit or 0.5 μms) is shown in figure 9(a), while the 5000 grit polish is shown in figure 9(b). The highly polished surface was observed to be near the optical limit (for observing surface variation) with only a few scratches visible. Comparatively the lower polish observes a significant increase in roughness. All electrode images (except for figure 9(b)) used a purely optical image. Figure 9(b) is observed with an imaging technique that uses multiple lighting angles to better indicate surface texture through shadows. The color of both

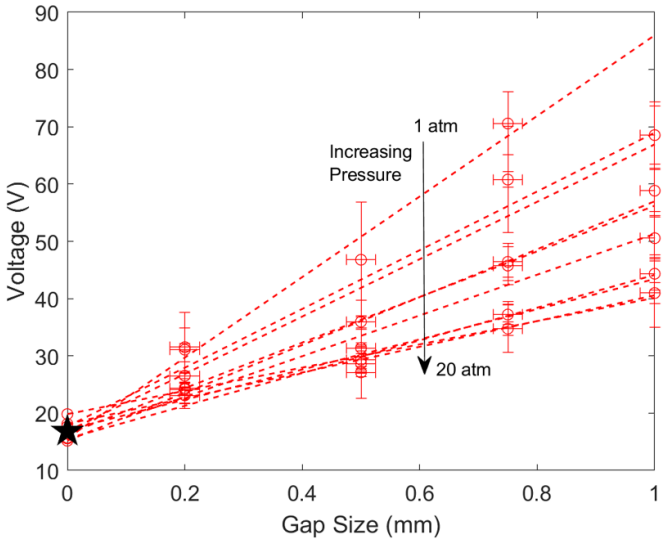

Figure 8. Voltage versus gap distance for arc discharge of stainless-steel electrode in air. The red circles are measured voltages, the black star is the zero-gap extrapolated voltage (i.e. voltage drop), the dashed lines are the linear extrapolation, and the error bars are associated with the experimental uncertainties.

figures 9(a) and (b) are observed to be uniform since they represent normal-use electrodes.

The heavy-use electrodes for both used polish levels are shown in figures 9(c) and (d). The full-color images are observed as this provides interesting information regarding the formation of oxide on the electrode surface as mentioned in the previous section. The color change observed after multiple discharges is assumed to be the buildup of oxidation on the surface. Friburg *et al* [69] provided data regarding the reflective colors of oxide on stainless steel. Based on this description the surface is fully coated with oxide at different layer thicknesses between 20 to 300 nm. This will completely change the composition observed by the plasma, which, alone, is enough to affect the work function and consequently the sheath formation. In addition, the roughness (while only observed comparatively) is seen to increase (especially the case for the 46 000 grit polish but also for the 5000 grit). This is inferred through observation of scanning electron microscope images provided by Friburg [69] which show the texture of the oxide layer is material that is flaking from the surface. This surface modification will likely produce an increased surface area over the freshly polished electrode.

The change from the normal-use 5000 grit (figure 9(b)) to the heavy-use (figure 9(d)) has a similar oxide formation to the 46 000 grit (figure 9(c)) where the color (and expected thickness) are comparable. The major difference is that some of the original surface variations from the 5000 grit are still visible where the oxide layers are thin (light blue to orange/red). On the other hand, the thickest oxide ($\sim$300 nm thick -white/grey color) is observed to completely obscure the markings of the 5000 grit. This would suggest that after a significant number of tests both electrodes will eventually reach the same condition (roughness and oxide thickness) regardless of the initial polish level.

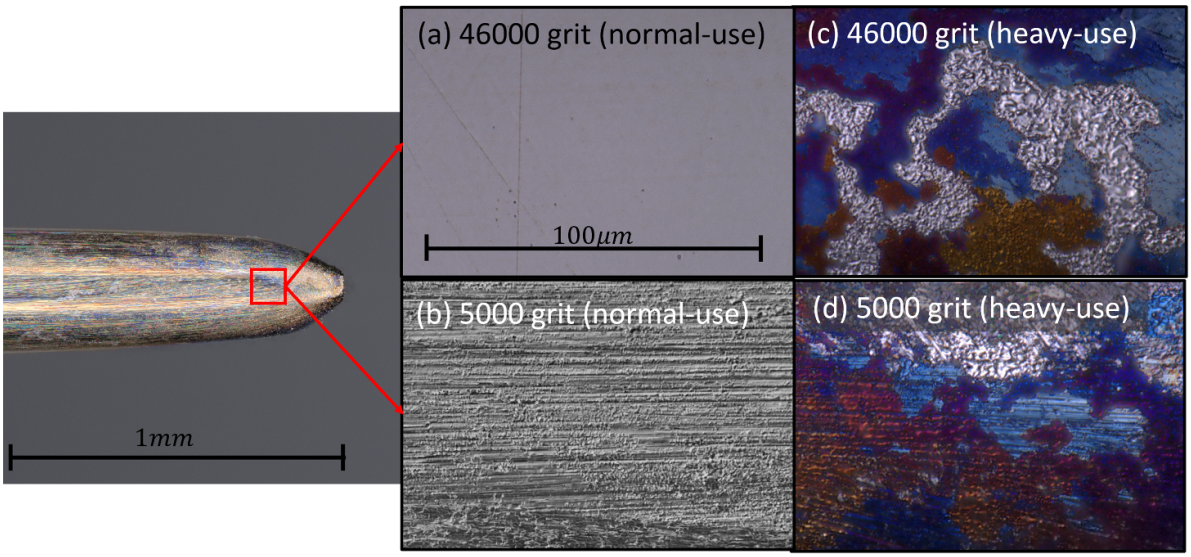

Figure 9. Electrode shape and quality for (a) 46 000 grit polish under normal-use, (b) 5000 grit polish under normal-use, (c) 46 000 grit polish under heavy-use, (b) 5000 grit polish under heavy-use. (Images are at x2500 Magnification-Keyence VHX-7000).

Table 4. Experimental ignition conditions.

Case number #	Composition	Pressure (atm)	Stored voltage	Voltage drop in glow (V)	Voltage drop in arc (V)	Percent arc	Discharge radius
1	Air	1	100	330	N/A	0%	0.5
2	Air	1	160	330	15-N/A	13%	0.5
3	Air	3	160	320	15-N/A	32%	0.3
4	Air	3	160	320	N/A	0%	0.3
5	Air	5	160	305	15-N/A	53%	0.3
6	$N_2 + CH_4$	1	160	348	15	10%	0.5
7	$N_2 + CH_4$	1	100	N/A	40	100%	0.3

4.4. Kernel propagation and modeling results

Table 4 provides the conditions of the presented experimental and modeling results. These conditions were selected to show a wide range of observed propagation characteristics that are a result of discharge mode (arc/glow), gas pressure, gas composition, and discharge current. The stored voltage (on the primary capacitor) represents the maximum current passed through the gap with 160 V resulting in a maximum of ∼0.8 A (see figure 2) and 100 V resulting in a max current of ∼0.5 A. The total possible energy stored by the ignition system is found to be on the order of several joules but there are many inefficiencies within the ignition circuit (i.e. transformer coils) that make this determination pointless for the spark analysis since the spark gap only sees a fraction of this energy. The voltage drop is the measured constant loss used for each spark condition, naturally the value changes depending on if the plasma is arc or plasma (section 4.2). The type of plasma for each case is also shown as a percentage, where the duration of the spark in arc discharge is presented against the total duration of the spark time (∼0.7 ms). The discharge radius is a parameter used in the DNS model which represents the size of the region in which the spark energy is dissipated (given the model is one dimensional). The initial conditions ($r_i$and T_i) are not reported as the effect on the overall result is minimal (see the following section). In general, the measured initial radius within the uncertainty of the measurement can be used along with a physical temperature value (300–1000 K).

In the following section, it is shown that the power input is the most important modeling factor. Other effects such as thermal conductivity terms or the boundary conditions show comparatively little change in the results. For this reason, the most important parameter to consider in the analysis is the sheath loss applied to the input power data. In addition, arc discharge represents a significant physical change to the experimental conditions (dimension and location of the power dissipation by plasma changes, affecting the dimensionality of the system), which is challenging to represent with these simplified models. The assumptions and results of the glow plasma are shown to be in greater agreement with the experimental results, once arc discharge is introduced, results are observed to significantly deviate from the experiment such that a 15 V sheath loss greatly overpredicts the experimental conditions (this is discussed further with the results in figure 15). Two model conditions are considered for the arc voltage drop: (1) 15 V, which would be the measured loss and on the same order of magnitude as other spark models previously

discussed, and (2) N/A condition that represents the entire spark energy removal if the arc does not affect the kernel boundary (this is equivalent to a voltage drop greater than ∼80 V). This will illustrate the potential range of solutions available during arc discharge assuming the loss is greater than the assumed voltage-drop. Of course, the entire removal of the arc is not physical so the case for the pure arc is observed with a larger drop which suggests there are additional phenomena that must be accounted for during the arc beyond the initial assumptions.

4.4.1. Model sensitivity. Logarithmic sensitivity analysis ($S = \mathrm{d}\left(\ln\left(r_{\mathrm{final}}\right)\right)/\mathrm{d}\left(\ln\left(x_i\right)\right)$) is performed for both models to assess the uncertainty of model parameters and inputs. The sensitivity determines the relative contribution of the change of a given model input, x_i, compared to the change in the final calculated kernel radius. The sensitivity is calculated using results from Case #1 and considers some of the major model inputs including; the initial radius and temperature of the kernel (T_i, r_i), the conductivity of the gas, k, (given mass gain is driven primarily by thermal conduction) the boundary conditions of the kernel (T_b or $\nabla\rho$, discussed further in section 4.4.3), and the value of sheath loss (variation in input energy).

The initial inputs, and r_i are shown to have an insignificant effect on the final radius, this suggests the modeling solution converges to a physical solution, where only the model results immediately following the initial conditions are affected by initial input variation. The sensitivity of thermal conductivity is important to determine since this transport property is utilized from literature for air and is not modified for alternate conditions. The sensitivity is larger but is not expected to be a major source of error. Future work may consider more detailed thermal conductivity should it be necessary.

The boundary criteria of the kernel constitute an interesting parameter to consider because there are to some degree associated with how each model physically interprets the observed kernel. In the 1D model, a temperature profile is calculated with respect to radius with the edge of the kernel represented by the max change in density $\nabla\rho_{\mathrm{max}}$. This value will be physically representative of the Schlieren system but there is no guarantee that this definition is the location measured when observing the kernel. The dependence of the final radius on the selected boundary condition can be determined if the boundary is assumed to vary around the max density gradient. Naturally, the sensitivity to this condition will increase toward the end of the experiment as the temperature diffuses further outward and the temperature (and density) profile flattens. As mentioned previously the 0D model assumes a linear temperature profile such that to define a boundary edge an isotherm must be selected. Just as in the DNS model the calculated radius changes if the boundary temperature, T_b, is varied, however, unlike the DNS model this parameter also defines the slope of the temperature gradient (and strength of mass gain through thermal conduction). It is suspected the sensitivity to the boundary is slightly lower than the DNS since this parameter partially defines the transport characteristics of the kernel (i.e. temperature and mass are more affected since the overall temperature profile is fixed unlike the fully solved temperature profile in the DNS model).

The voltage drop is markedly the most significant input parameter. This value represents the input power to the model and should be the first value to consider for potential errors in the result. An example of the model variation is shown in figure 10(b) with the final model radius presented for the conductivity, boundary condition, and voltage drop. Initial conditions are not displayed as they are insignificant.

4.4.2. Model validation. To ascertain the validity of both models, the results of the kernel mass and temperature are examined and presented in figures 11 and 12. The results of both modeling methodologies should physically be similar to each other and be physically realistic with available experimental data. Calculated and measured temperatures of similar spark discharges are shown in figure 11 against the discharge current. As the current increases the overall intensity and temperature of the kernel should rise as shown in both sets of data.

Available literature temperature data [33, 34, 72–78] for similar conditions is also plotted. The temperature should be carefully defined as this value can be interpreted in a few ways. The actual temperature of the ignition kernel has a profile radially, which, when measured using an optical emission method would not be capable of distinguishing emissions detected along the axis of the detector's line of sight. For this reason, when comparing the model results to experimental data, the DNS radially resolved temperature can be utilized to calculate a similar measurement (path averaged) through the center of the kernel (Green dashed line). The literature data reported are the rotational gas temperatures for similar spark conditions (1 atm, air, glow). The comparison shows the model prediction is slightly higher than the available data. There are a couple of explanations for this, (1) The experimental measurement path has some thickness: in the ideal case where the maximum temperature is precisely at the center of the kernel will result in a lower temperature if the measurement has a thickness (or a zero thickness line through the center will result in a larger value), (2) There is variation in kernel temperature through the axis of the electrode [34]: if a more detailed plasma structure is considered (positive column, negative glow, dark space), the exact measurement location within the plasma for these experiments may result in different values from this simple model, (3) The uncertainty of these reported temperatures are often several hundred degrees K. Given the many possible sources of variation between available experimental conditions, the difference of ∼500 K observed at the maximum current is suggested to be a reasonably good prediction of the kernel temperature. The temperature calculated is both physically possible and realistic while also observing the expected trend as current (and spark energy) increases. Additionally, close agreement is found between both model temperature

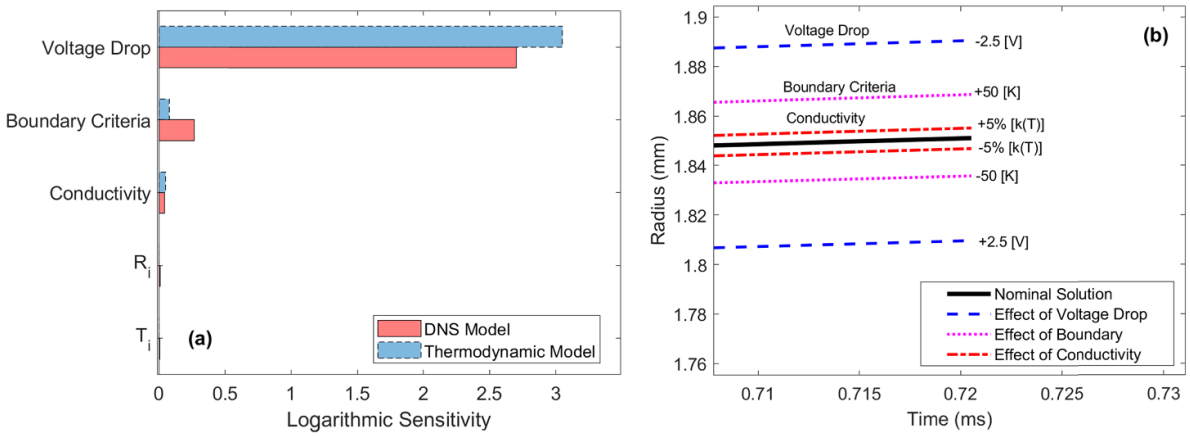

Figure 10. (a) Sensitivity of the radius to relevant model inputs and (b) effect of significant parameters on radius.

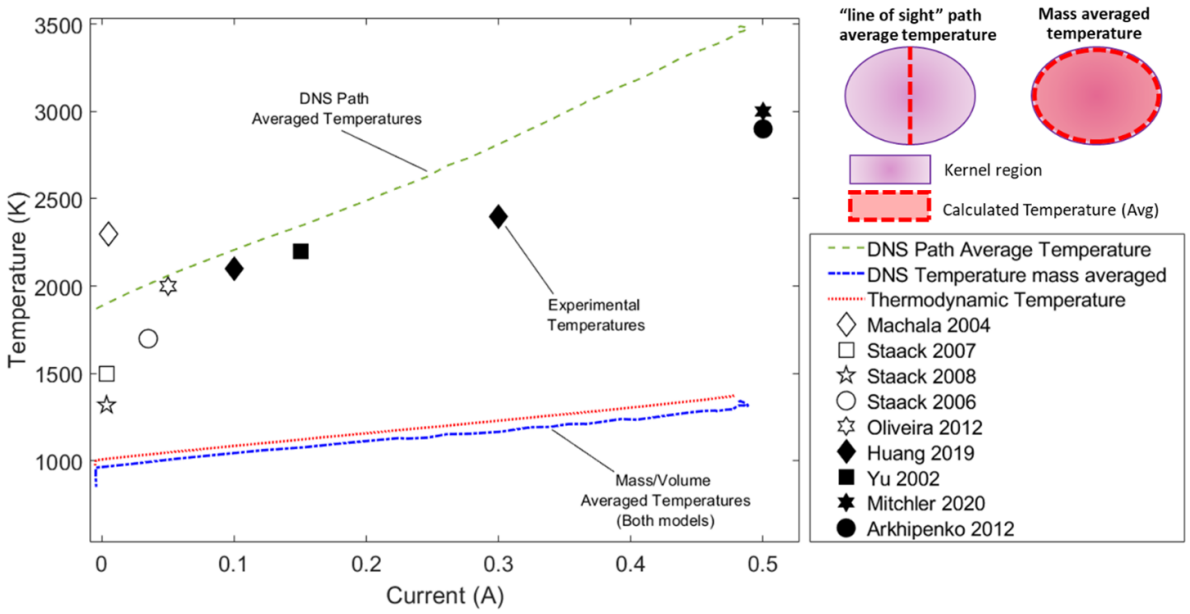

Figure 11. Characteristic model temperature with experimental rotational gas temperatures [33, 34, 72–78] in atmospheric air (Case #1).

calculations. To accurately compare the temperature calculated by the Thermodynamic model (given the model is not radially resolved), a 'mass-averaged' temperature for both models is compared where the entire kernel is included in the measurement.

The mass gain in figure 12 also shows good agreement. The mass gain (through thermal conduction) is defined in the thermodynamic model using a linear temperature profile. In the following section, the DNS-calculated temperature profile is displayed which shows a non-trivial profile as conduction extends beyond the discharge region. It is these discharge profiles which might suggest the linear profile is indeed the be approximation without realizing a full 1D model. The rate of change of mass matches toward the end of discharge when diffusional effects (not input energy) are the most significant. The discrepancy in the mass profile of the two models is expected to be a result of the simplified thermal conduction with the best agreement occurring when the DNS model temperature is better approximated with a linear profile (near the middle of the discharge).

4.4.3. DNS results. Additional results of the DNS model are shown in figure 13 where samples of the radial temperature profile over time and the conditions at the kernel boundary are shown. This provides some key insight into the kernel characteristics. Namely, a more accurate understanding of how the current (rises and falls over time see figure 13) affects the maximum and average kernel temperature (and consequently the rate of kernel propagation). In figure 13(a), the temperature is captured at 6 points where three are under rising current conditions and three are under a falling condition. Both the maximum and averaged temperatures will rise and fall with the current as this indicates a significant change in total power

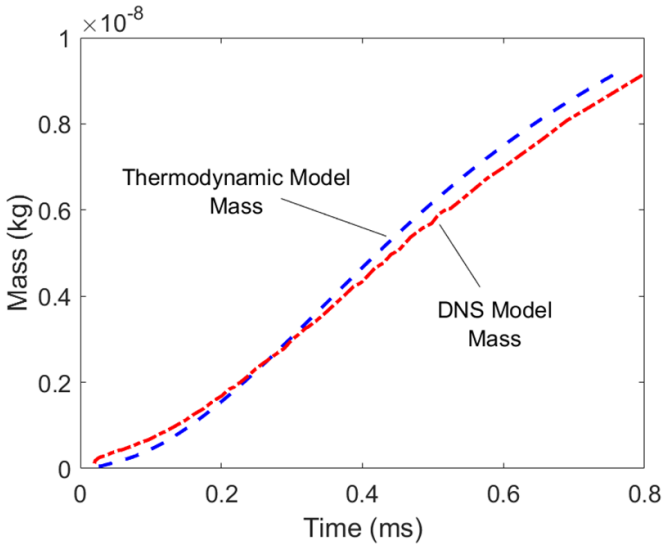

Figure 12. Calculated total kernel mass of both models in atmospheric air (case #1).

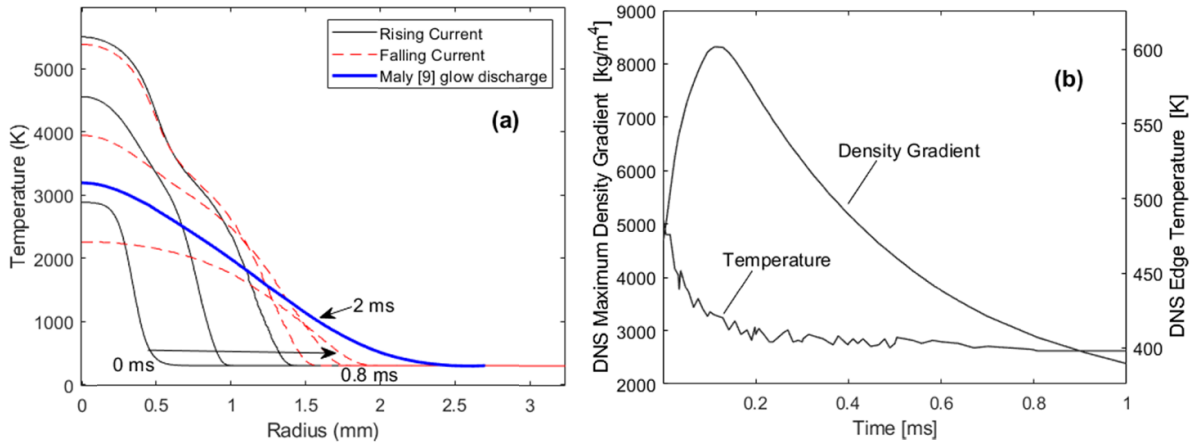

Figure 13. (a) DNS kernel radial temperature profile and (b) DNS kernel boundary conditions.

deposited (for glow discharge). In addition, the conditions at the DNS kernel boundary are presented in figure 13(b) and are useful results for comparison to the thermodynamic model as well as to understand the assumptions used in the definition of the simplified thermal conduction for the thermodynamic model.

The first significant observation for figure 13(a) is the kernel temperature profile towards the end of discharge, has a reduced gradient. This is observed as less defined experimental kernel boundary when the kernel reaches the maximum size and will result in an increase in uncertainty of the edge location as thermal conduction (with zero additional energy) becomes the only mechanism increasing the kernel radius. The density gradient at the edge (maximum) is presented in figure 13(b) to illustrate this point.

The temperature at the edge selected from the DNS model is also presented in figure 13(b) to show that the isotherm chosen to define the kernel boundary and temperature gradient in the thermodynamic model is similar to the DNS model results (i.e. the edge of the thermodynamic model kernel can accurately be assumed to exist at an isotherm). The temperature profile calculated is compared to the results of Maly [9]. Maly calculates a glow discharge that has a maximum temperature of ∼3000 K after a long duration (2 ms). The exact magnitude and shape of the temperature profile is highly dependent on many spark characteristics (duration, energy, gap size…) however the general solution shown in figure 13(a) is in general similar. This profile in Maly [9] is however associated with the minimum ignition criteria defined in his work which is exceeded in the present work in a much shorter spark duration. Here, the temperature and overall radius are observed to vary greatly as the energy within the glow regime changes.

4.4.4. Model application. Modeling results of the conditions outlined in table 4 are shown in figures 14 and 15. As mentioned previously in section 4.4 the optimal observed

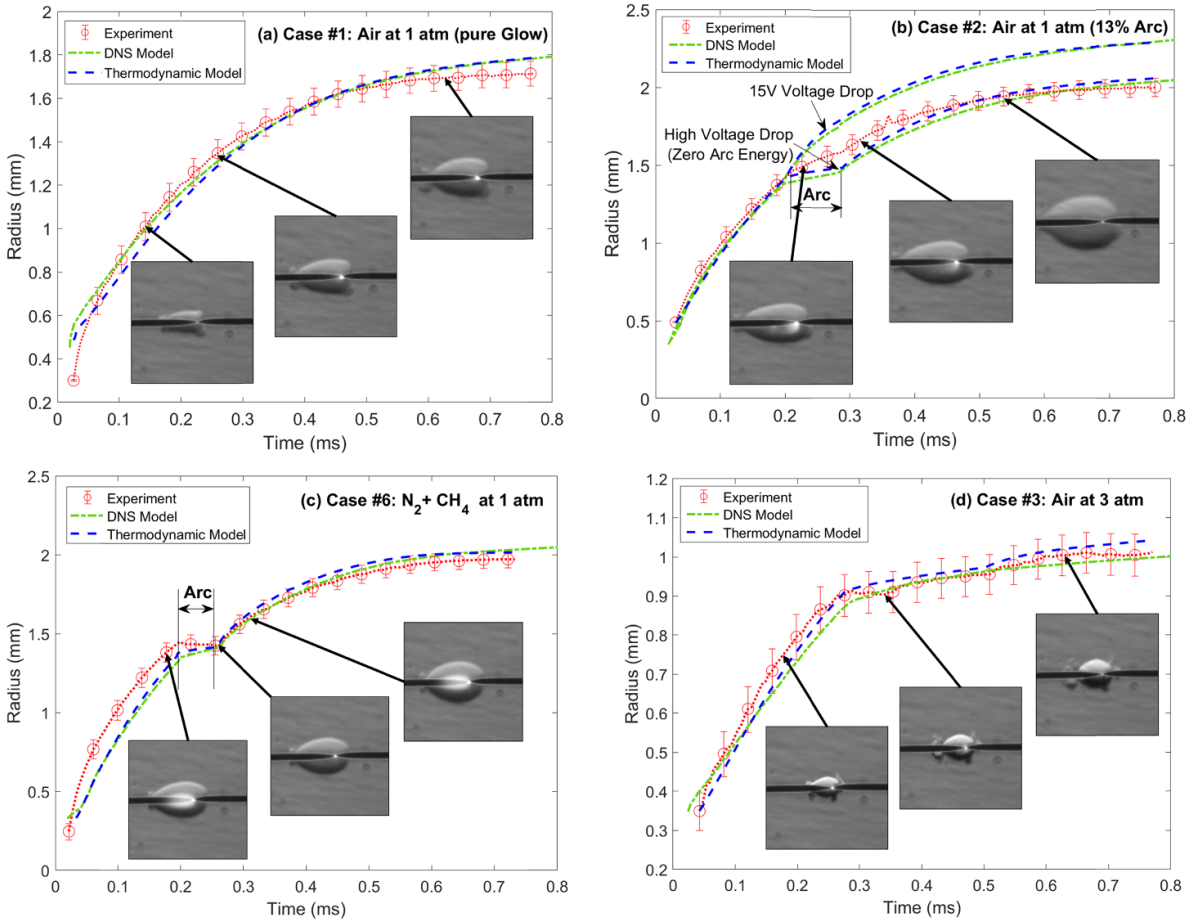

Figure 14. Model results for (a) pure glow discharge at 1 atm in the air (case #1), (b) glow discharge with 13% arc discharge at 1 atm in the air (case #2), (c) glow discharge with physically small arc discharge in $N_2 + CH_4$ (case #6), and (d) glow and arc discharge at 3 atm in the air (case #3).

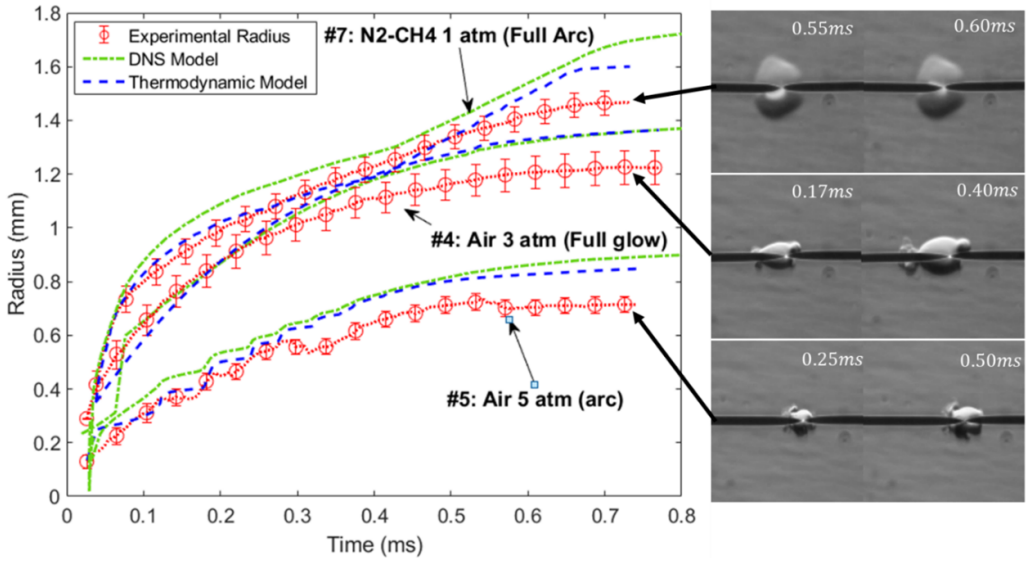

Figure 15. Further model results with pure arc discharge in $N_2 + CH_4$ at 1 atm (case #7), pure glow discharge at 3 atm in the air (case #4), and arc-glow at 5 atm in the air (case #5). (Pure glow at 5 atm is nearly impossible to achieve.).

kernel condition is pure glow discharge with results shown in figure 14(a). The model result in Case #1 is shown to predict the overall magnitude of the propagation but a discrepancy between both models and the experimental measurements is noted. This deviation in propagation profile from experimental results is expected to be a product of the assumptions made for the loss measurement values and is discussed in detail in the following section. The glow discharge conditions naturally cannot be maintained for all conditions, therefore, discharge containing some form of arc discharge is shown in figures 14(b)–(d).

The arc plasma is to some degree random, so several possible conditions are presented. In figure 14(b), the same atmospheric condition as figure 14(a) is shown with just a small fraction of arc discharge. At the moment of arc transition, the propagation rate of the kernel observes a sudden change (the arc region is shown between two vertical lines). The power measured through the voltage and current waveform of course changes with the arc transition however the expected non-thermal loss of 15 V greatly overpredicts the measured kernel. This measured value is in the same order as the theoretical voltage drops (where the cathode drop is related to the ionization potential of the electrode (∼7.9 V) and the anode drop is comparable to the work-function (∼4.4 V) of the electrode [32]. In the case of figure 14(b), both the originally proposed model loss (∼15 V drop) and the condition with zero arc energy input (high voltage drop) are shown, which indicates the full potential range of model results. The experimental results fall somewhere in between these values which suggest there are additional phenomena that are not accounted for by the present models. One explanation is the simplification of arc discharge geometry. For example, arc discharge can exist off axis that results in kernel growth that is not fully captured by the optical measurement, meaning the total effect that the spark has on the kernel is not observed.

On the other hand, the size of the plasma region can vary greatly. In figure 14(b) the cathode spot of the arc is visible and is almost the same length as the glow discharge (although the overall plasma size is limited to a much smaller diameter). The arc of this length appears to cause significant growth to the once glow-filled kernel. In the case of figure 14(c), the arc plasma is observed to exist solely between the tips of the electrode. This reduction in size compared to figure 14(b) both reduces the measured power but also appears to result in an arc that has almost no effect on the kernel size with complete kernel stagnation. It would be inappropriate with only this knowledge of the plasma size to assume the loss to the sheath formation is higher than the measured values. Rather, the energy heating of the gas must form a more complicated temperature profile with higher center temperatures, where the thermal conduction to the kernel boundary must take additional time and energy as compared to the glow discharge. A realistic modeling of this effect would require at least the resolution for the radial dimensions such as what is done in the DNS model where the size of the energy deposition can be specified. For the case with glow and arc discharges, the evidence is inconclusive to determine the accuracy of the arc loss value since the actual arc plasma dimensions as compared to the glow plasma. Further insight can be found by considering a condition of pure arc discharge since there would be no influencing effects of glow geometry.

Additional results are shown in figure 14(d) for kernel propagation at 3 atm. This condition has considerable arc propagation seen in the plateau of the data and a short burst of glow discharge towards the end seen with a final bump at 0.65 ms. Here the thermodynamic model assumes a larger loss than the 15 V. However, for the DNS model a smaller discharge radius is used suggesting that the dimensionality of arc discharge needs to be accounted for (especially when preceded by glow).

Further results are presented in figure 15 where, most interestingly, a kernel with nearly pure arc discharge is observed. Without a preceding glow discharge, the kernel boundary is known to be directly the result of the arc plasma. Despite the lack of the glow discharge kernel, a larger sheath loss (∼40 V) is used to result in a better fit. The author concludes that this is potentially a result of one of two effects: (1) the arc discharge may not be fully symmetric resulting in unmeasured heated volumes in front or behind the kernel, or (2) there is some other loss mechanism which is not accounted.

In defense of the second explanation, when the cathode spot is beyond the electrode tip, the arc plasma must still be adjacent to the highly electronegative wire. To maintain the plasma region some additional sheath may form outside of the cathode spot to isolate the plasma [66], this sheath would not be present in the arc sheath measurement since discharge between the tips was only used. As observed in Benelov [79], the sheath formation can be potentially very complicated unlike the simplistic approach taken in this work. This potential additional sheath would change with length and is highly dependent on the electrode geometry, complicating future analysis. On the other hand, temperatures are approaching the threshold where radiation becomes significant. In general, an average kernel temperature is used to calculate radiation loss, but a more detailed space-varying result may show an additional loss at the hottest part of the arc kernel near the center.

The other conditions shown in figure 15 include pure glow discharge at 3 atm and arc-glow discharge at 5 atm in the air. A lower sheath loss is selected as the pressure increases. Compared with the 1 atm at pure glow, similar errors are seen with some overprediction at the final radius. This is explained in the following section as the analysis of pure glow discharge can be more definitive since this propagation is more predictable. At 5 atm, there is significant arc discharge where, again, the loss is found to be larger than expected (∼45 V).

4.4.5. Interpretation of results. The results between the modeling and experiment are noted not to be a perfect match. The difference between the model and experiment is plotted in figure 16 for selected cases. The discrepancy is observed to be on the order of 15% of the experimental radius. Additionally, a structure is noted for most of the experimental results

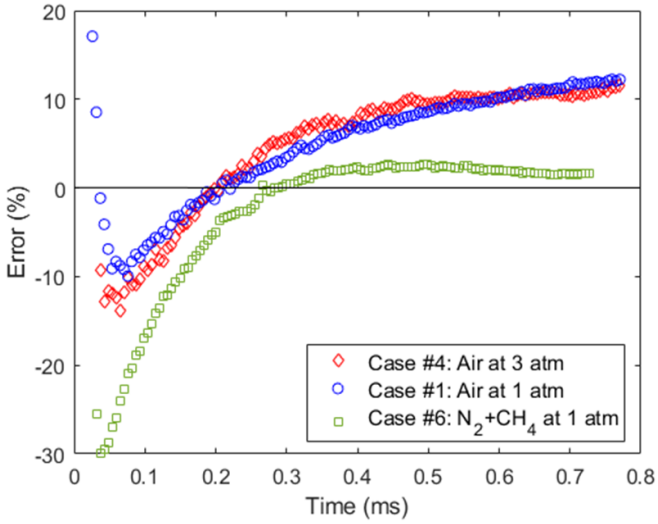

Figure 16. Residuals showing the discrepancy between model results and experimental data.

where early time is underpredicted with the final radius overpredicted.

Several potential sources were explored to explain this difference including ideas such as heat conduction to the electrode, larger kernel surface areas from non-spherical shapes, and inaccurate edge detection as the edge density gradient (figure 13(b)) at the end discharge reduces. However, the sensitivity (figure 10) to these parameters is not significant enough to cause the observed discrepancies. It is proposed that the primary source is most likely a result of the input power, specifically the sheath measurements.

For simplicity in measurement and modeling analysis, a constant sheath loss was assumed early in this work. This assumption has been made in other modeling works [12, 26, 37, 39] and most empirical sheath drop values for glow discharge [32] that are often used are for a normal glow and/or have high uncertainties (especially given the many parameters which affect discharge). This assumption is likely inaccurate (at least for the discharge observed in this work), especially noticeable when observing the kernel propagation with high temporal and spatial resolution. For engine experiments, averaged and approximate values can be acceptable, and when the discharge is less likely glow.

Since the model is primarily sensitive to the input energy, the sheath measurement should be considered with greater scrutiny. A reasonable explanation is found when the current density at the cathode fall was characterized (figure 17) by measuring the size of the luminous region (where possible). For a condition with a constant sheath drop, the current density should remain constant. If the current density changes, the voltage drop should be expected to change as well.

To observe the trend of current density, the discharge area vs time was estimated for glow discharge of a tip-to-tip geometry from the available experimental results. To ensure the observed trend was accurate, the current density was also measured using a flat plate electrode which can more easily observe the sheath diameter. For both conditions, the current density was shown to decrease with time, which suggests that the glow discharge is abnormal [80]. The abnormal discharge is a result of the transient nature of the current rate of change. When the discharge area is plotted against the current, a phase shift of 0.1 ms is observed for the flat plate discharge. This is similar (although an order of magnitude larger) to the transient time (0.1 μs) of Nahemow and Wainfan [81], which observed the glow discharge at a much lower pressure of 10 Torr. Since the discharge never reaches a steady state current and the current density is shown to change, a more accurate voltage drop measurement should vary with time.

Cathode temperature is another factor that likely affects sheath formation. Arkhipenko *et al* [50] showed that the current density changes for uncooled electrodes which supports the theory that the voltage drop changes with time. The small mass of the electrode along with rapid surface heating would suggest the electrode temperature seen by the plasma rises rapidly.

Further analysis can be done by reversing the model calculation to make the radius the input and the spark power the output. This results in the optimal input 'perfectly match' the kernel propagation. Additionally, if the sheath formation is truly the primary mechanism for non-thermal loss, then this result could represent the real, time-varying sheath drop (assuming the models accurately represent the system, and the radius is absolutely accurate). Regardless, the observed trend of the calculated sheath-drop vs the current density appears to be related. The initial curve for the first 0.1 ms is expected to be from the initial formation of glow discharge where the current density should really asymptote to infinity (area starts at zero, where time and spatial resolution prevent higher accuracy of current density at the early time). This early time might represent the initial stabilization of the glow plasma where electrode surface temperature and ionization of the gas must stabilize and take place.

Once stabilized the calculated sheath drop increases linearly just as the current density decreases. The sheath

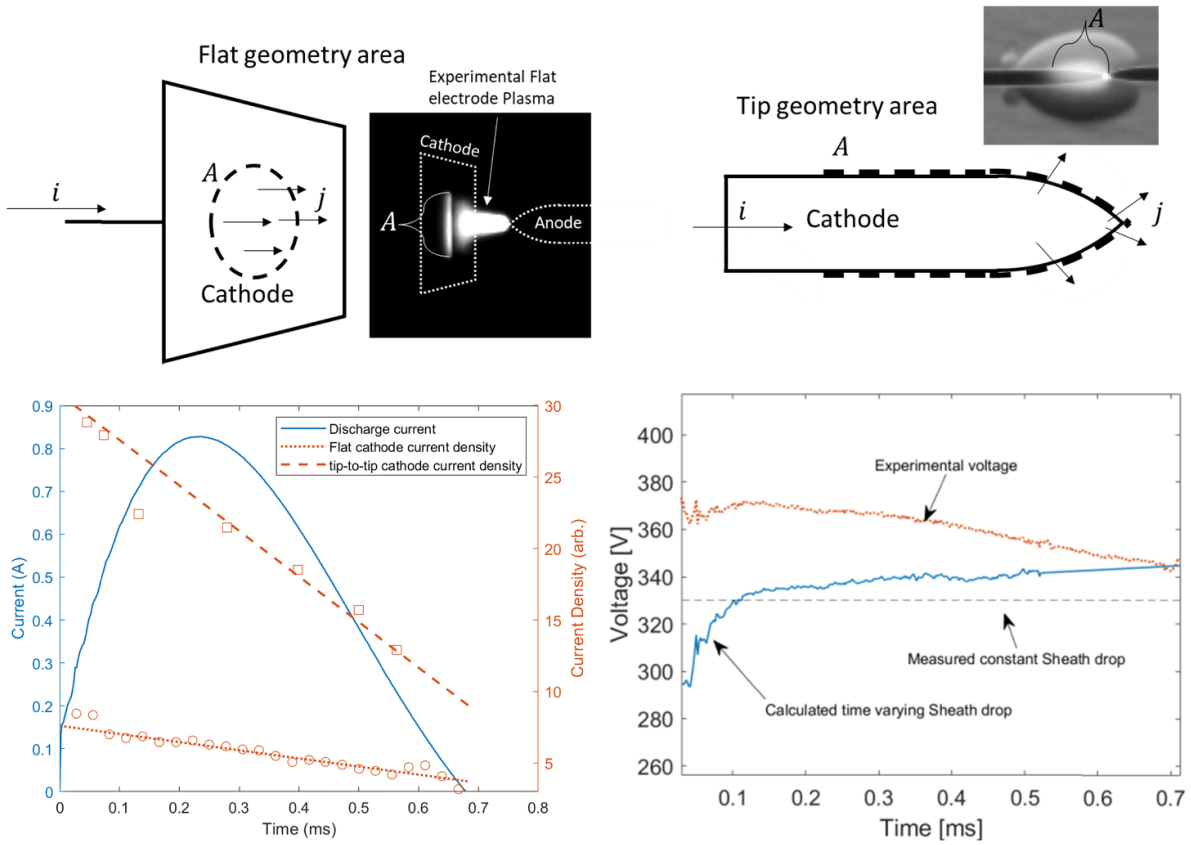

Figure 17. Expected source of residuals. (top) diagram of current density measurements (bottom left) characteristic current density of observed spark and (bottom right) optimal power input to fit final radius (glow discharge).

change in current density is seen to be accentuated by the tip geometry where the plasma must grow in length. For the tip geometry observed the plot of sheath drop vs current density follows a linear trend of approximately, $V_f = -0.92\,[\mathrm{V}\cdot\mathrm{cm}^2\,\mathrm{A}^{-1}]\cdot j[\mathrm{A\,cm}^{-2}] + 358\,[\mathrm{V}]$. This trend of course means little in terms of other geometries or discharge conditions, however, characterizing this curve under different ignition ranges may provide additional insights and improved model accuracy in future research.

5. Conclusions

An investigation of super-atmospheric pressure spark discharge has been conducted and involved a comprehensive study of the morphology of plasma and kernel starting with breakdown through the diffusive glow and arc plasmas. A framework for accurately reproducing the radial propagation of thermal spark plasma utilizing the input spark energy has been developed using two modeling approaches.

Reasonable agreements were found between predictions of the two models as well as between model predictions and experimental results. The models reproduce available literature kernel temperatures and the kernel radius is also shown to be within ∼15% of the experimental radius. The temperature and mass of the 0D thermodynamic model are also comparable to the DNS model.

The benefit of utilizing both modeling approaches is greater understanding and confidence in modeling. The DNS model provides additional detail regarding properties inside of the kernel and additional results to validate against experimental data. The thermodynamic model given the greater simplicity can allow for wider use and can be compared and validated against the DNS model and experimental conditions. The agreement observed here (between models) may not be the case for other conditions (i.e. higher pressure, other geometries, heavy arc discharge), but development of the DNS modeling can help produce develop accurate simplified models in such cases given additional experimental data in future studies.

Simplification of the plasma losses associated the sheath formation to a constant value is thought to be the most significant source of discrepancy between modeling and experimental data. And the sheath formation must be expected to be transient for the entire discharge if the rate of current change is significantly large.

Arc discharge was found to further deviate from the expected energy from potentially further reasons including changes in plasma geometry and additional losses based on the shape of the electrode in comparison to the plasma region.

Important conclusions from the work include:

1. The value of voltage-drop, measured with the experimental technique proposed, is expected to be at most

a nominal value for the pulsed discharge (where effective length, electrode temperature, and current density are changing and not accounted for). As a result, more detailed modeling for arc discharge (or more rigorously controlled experimental arc discharge) is required to improve modeling accuracy in this regime.
2. For the small electrode in glow discharge, it is agreed that the cathode fall is the primary non-thermal loss (conduction to electrode/radiation are negligible).
3. Simplification to zero-dimension using a linear temperature profile appears to be acceptable. Additionally, the spherical approximation of the kernel is also acceptable for the glow-arc discharge.
4. The assumption of normal glow discharge is not necessarily acceptable for all discharge types. The current density should always be measured to ensure a constant loss can be applied for modeling results.

Future work to improve results will consider a changing voltage drop, $V_{\text{fall}}\,(T_{\text{elec}}, t)$, as a function of electrode temperature and time (or current density). It is proposed that this could be done potentially with experimental data if and alternative ignition circuit design is used with a constant (or nearly constant) current profile. Alternatively, if a time-resolved plasma model (such as [82] or [83]) is implemented, it could provide insight into how sheath formation changes with time and improve the results presented here.

In summary, further understanding of arc discharge and its realization to kernel propagation deserve further studies. Also, incorporating time-resolved glow discharge (or creating a spark that has a constant cathode fall) should be accomplished.

Data availability statement

All data that support the findings of this study are included within the article (and any supplementary files).

ORCID iD

Omid Askari https://orcid.org/0000-0003-0050-6768

References

[1] Zembi J, Cruccolini V, Mariani F, Scarcelli R and Battistoni M 2021 Modeling of thermal and kinetic processes in non-equilibrium plasma ignition applied to a lean combustion engine *Appl. Therm. Eng.* **197** 117377
[2] Bogaerts A and Centi G 2020 Plasma technology for CO_2 conversion: a personal perspective on prospects and gaps *Front. Energy Res.* **8** 111
[3] Ju Y and Sun W 2015 Plasma assisted combustion: dynamics and chemistry *Prog. Energy Combust. Sci.* **48** 21–83
[4] Haertel B, von Woedtke T, Weltmann K D and Lindequist U 2014 Non-thermal atmospheric-pressure plasma possible application in wound healing *Biomol. Ther.* **22** 477
[5] Economou D J 2014 Pulsed plasma etching for semiconductor manufacturing *J. Phys. D: Appl. Phys.* **47** 303001
[6] Askari O, Wang Z, Vien K, Sirio M and Metghalchi H 2017 On the flame stability and laminar burning speeds of syngas/O_2/he premixed flame *Fuel* **190** 90–103
[7] Askari O, Moghaddas A, Alholm A, Vien K, Alhazmi B and Metghalchi H 2016 Laminar burning speed measurement and flame instability study of H_2/CO/air mixtures at high temperatures and pressures using a novel multi-shell model *Combust. Flame* **168** 20–31
[8] Askari O, Vien K, Wang Z, Sirio M and Metghalchi H 2016 Exhaust gas recirculation effects on flame structure and laminar burning speeds of H_2/CO/air flames at high pressures and temperatures *Appl. Energy* **179** 451–62
[9] Maly R 1981 Ignition model for spark discharges and the early phase of flame front growth *Symp. Combust.* **18** 1747–54
[10] Kravchik T, Sher E and Heywood J B 1995 From spark ignition to flame initiation *Combust. Sci. Technol.* **108** 1–30
[11] Kelley A P, Bechtold J K and Law C K 2012 Premixed flame propagation in a confining vessel with weak pressure rise *J. Fluid Mech.* **691** 26–51
[12] Maly R and Vogel M 1979 Initiation and propagation of flame fronts in lean CH_4-air mixtures by the three modes of the ignition spark *Symp. Combust.* **17** 821–31
[13] Deak N, Bellemans A and Bisetti F 2020 Plasma-assisted ignition of methane/air and ethylene/air mixtures: efficiency at low and high pressures *Proc. Combust. Inst.* **38** 6551–8
[14] Askari O, Elia M, Ferrari M and Metghalchi H 2017 Auto-ignition characteristics study of gas-to-liquid fuel at high pressures and low temperatures *Trans.ASME,J.Energy Resour.Technol.* **139** 012204
[15] Yu G, Askari O and Metghalchi H 2018 Theoretical prediction of the effect of blending jp-8 with syngas on the ignition delay time and laminar burning speed *Trans. ASME, J. Energy Resour. Technol.* **140** 012204
[16] Zare S, Lo H W and Askari O 2020 Flame stability in inverse coaxial injector using repetitive nanosecond pulsed plasma *Trans. ASME, J. Energy Resour. Technol.* **142** 082101
[17] Zare S, Lo H W, Roy S and Askari O 2020 On the low-temperature plasma discharge in methane/air diffusion flames *Energy* **197** 117185
[18] Mulla I A, Chakravarthy S R, Swaminathan N and Balachandran R 2016 Evolution of flame-kernel in laser-induced spark ignited mixtures: a parametric study *Combust. Flame* **164** 303–18
[19] Zhang J, Hu E, Gao Q, Yin G and Huang Z 2021 Shock wave propagation and flame kernel morphology in laser-induced plasma ignition of $Ch_4/O_2/N_2$ mixture *Energies* **14** 7976
[20] Poggie J and Leonov S 2015 Plasma aerodynamics: current status and future directions *Aerosp. Lab. J.* **10** 1–6
[21] Likhanskii A V, Shneider M N, Macheret S O and Miles R B 2008 Modeling of dielectric barrier discharge plasma actuator in air *J. Appl. Phys.* **103** 053305
[22] Im S, Do H and Cappelli M A 2010 Dielectric barrier discharge control of a turbulent boundary layer in a supersonic flow *Appl. Phys. Lett.* **97** 041503
[23] Bruggeman P J, Iza F and Brandenburg R 2017 Foundations of atmospheric pressure non-equilibrium plasmas *Plasma Sources Sci. Technol.* **26** 123002
[24] Zare S, Roy S, El Maadi A and Askari O 2019 An investigation on laminar burning speed and flame structure of anisole-air mixture *Fuel* **244** 120–31
[25] Askari O, Elia M, Ferrari M and Metghalchi H 2017 Cell formation effects on the burning speeds and flame front area of synthetic gas at high pressures and temperatures *Appl. Energy* **189** 568–77
[26] Ziegler G F W, Wagner E P and Maly R R 1985 Ignition of lean methane-air mixtures by high pressure glow and ARC discharges *Symp. Combust.* **20** 1817–24

[27] Kono M, Kumagai S and Sakai T 1977 The optimum condition for ignition of gases by composite sparks *Symp. Combust.* **16** 757–66
[28] Bane S P M, Ziegler J L and Shepherd J E 2015 Investigation of the effect of electrode geometry on spark ignition *Combust. Flame* **162** 462–9
[29] Kim K and Askari O 2019 Understanding the effect of capacitive discharge ignition on plasma formation and flame propagation of air-propane mixture *Trans.ASME,J.Energy Resour.Technol.* **141** 082201
[30] Loeb L B and Meek J M 1940 The mechanism of spark discharge in air at atmospheric pressure. I *J. Appl. Phys.* **11** 438–47
[31] Gambling W A and Edels H 1954 The high-pressure glow discharge in air *Br. J. Appl. Phys.* **5** 36–39
[32] Cobine J D 1942 *Gaseous Conductors, Theory and Engineering Applications* (New York: Dover)
[33] Arkhipenko V I, Kirillov A A, Safronau Y A, Simonchik L V and Zgirouski S M 2012 Plasma non-equilibrium of the DC normal glow discharges in atmospheric pressure atomic and molecular gases *Eur. Phys. J.* D **66** 252
[34] Michler T, Toedter O and Koch T 2020 Measurement of temporal and spatial resolved rotational temperature in ignition sparks at atmospheric pressure *Automot. Eng. Technol.* **5** 57–70
[35] Jenkins J and Jones T B 1957 Glow-arc transition in current-stabilized electrical discharges *J. Appl. Phys.* **28** 663–8
[36] Venkattraman A 2013 Cathode fall model and current-voltage characteristics of field emission driven direct current microplasmas *Phys. Plasmas* **20** 113505
[37] Lim M T, Anderson R W and Arpaci V S 1987 Prediction of spark kernel development in constant volume combustion *Combust. Flame* **69** 303–16
[38] Sher E, Ben-Ya'Ish J and Kravchik T 1992 On the birth of spark channels *Combust. Flame* **89** 186–94
[39] Kim J and Anderson R W 1995 Spark anemometry of bulk gas velocity at the plug gap of a Firing engine *SAE Technical Papers* (SAE International) (https://doi.org/10.4271/952459)
[40] Eisazadeh-Far K, Parsinejad F, Metghalchi H and Keck J C 2010 On flame kernel formation and propagation in premixed gases *Combust. Flame* **157** 2211–21
[41] Lu H, Liu F, Wang K, Xu G and Curran H J 2021 Numerical study on the minimum ignition energy of a methane-air mixture *Fuel* **285** 119230
[42] Shaffer J, Askari O and Zare S 2022 Electrode design for thermal and nonthermal plasma discharge inside a constant volume combustion chamber *Trans.ASME,J.Energy Resour.Technol.* **144** 082306
[43] Iwasaki S Automotive ignition systems *Google Patents US4733646A* (available at: https://patents.google.com/patent/US4733646A/en) (Accessed 15 March 2021)
[44] Traldi E, Boselli M, Simoncelli E, Stancampiano A, Gherardi M, Colombo V and Settles G S 2018 Schlieren imaging: a powerful tool for atmospheric plasma diagnostic *EPJ Tech. Instrum.* **5** 4
[45] Zare S and Askari O 2022 Mode transition and uncertainty analysis of repetitive nanosecond pulsed discharge *J. Electrostat.* **118** 103736
[46] Swett C C 1951 *NACA research memorandum spark ignition of flowing gases II-effect of electrode parameters on energy required to ignite a propane-air mixture* (Cleveland, OH: NACA)
[47] Keck J C 1981 Thermal boundary layer in a gas subject to a time dependent pressure *Lett. Heat Mass Transfer* **8** 313–9
[48] Billoux T, Cressault Y, Teulet P and Gleizes A 2012 Calculation of the net emission coefficient of an air thermal plasma at very high pressure *J. Phys.: Conf. Ser.* **406** 012010
[49] Ko Y and Anderson R W 1989 Electrode heat transfer during spark ignition *SAE Technical Papers* (https://doi.org/10.4271/892083)
[50] Arkhipenko V I, Kirillov A A, Safronau Y A, Simonchik L V and Zgirouski S M 2008 Influence of cathode temperature on the parameters of an atmospheric pressure Dc glow discharge *Plasma Sources Sci. Technol.* **17** 045017
[51] Kawahara N, Hashimoto S and Tomita E 2017 Spark discharge ignition process in a spark-ignition engine using a time series of spectra measurements *Proc. Combust. Inst.* **36** 3451–8
[52] Aragón C and Aguilera J A 2008 Characterization of laser induced plasmas by optical emission spectroscopy: a review of experiments and methods *Spectrochim. Acta* B **63** 893–916
[53] Askari O 2018 Thermodynamic properties of pure and mixed thermal plasmas over a wide range of temperature and pressure *Trans.ASME,J.Energy Resour.Technol.* **140** 032202
[54] Askari O, Beretta G P, Eisazadeh-Far K and Metghalchi H 2016 On the thermodynamic properties of thermal plasma in the flame kernel of hydrocarbon/air premixed gases *Eur. Phys. J.* D **70** 159
[55] Capitelli M, Colonna G, Gorse C and D'Angola A 2000 Transport properties of high temperature air in local thermodynamic equilibrium *Eur. Phys. J.* D **11** 279–89
[56] Lawson R, Gururajan V, Movaghar A and Egolfopoulos F N 2021 Autoignition of reacting mixtures at engine-relevant conditions using confined spherically expanding flames *Proc. Combust. Inst.* **38** 2285–93
[57] Richtmyer R D and Morton K W 1994 *Difference Methods for Initial-Value Problems* 2nd edn (Malabar, FL: Krieger Publishing Co.)
[58] Goodwin D, Moffat H, Schoegl I, Speth R and Weber B Cantera: an object-oriented software toolkit for chemical kinetics, thermodynamics, and transport processes (available at: https://cantera.org/community.html#citing-cantera)
[59] Frendi A and Sibulkin M 1990 Dependence of minimum ignition energy on ignition parameters *Combust. Sci. Technol.* **73** 395–413
[60] Chen Z and Ju Y 2009 Studies on the Initiation, Propagation, and Extinction of Premixed Flames *Doctoral Dissertation* Princeton University
[61] Hindmarsh A C, Brown P N, Grant K E, Lee S L, Serban R, Shumaker D E and Woodward C S 2005 SUNDIALS: suite of nonlinear and differential/algebraic equation solvers *ACM Trans. Math. Softw.* **31** 363–96
[62] Park C 1993 Review of chemical-kinetic problems of future NASA missions, I: earth entries *J. Thermophys. Heat Transfer* **7** 385–98
[63] Smith G P, Tao Y and Wang H Foundational fuel chemistry model version 1.0 (FFCM-1) (available at: http://nanoenergy.stanford.edu/ffcm1) (Accessed 20 August 2022)
[64] Eichwald O, Yousfi M, Hennad A and Benabdessadok M D 1997 Coupling of chemical kinetics, gas dynamics, and charged particle kinetics models for the analysis of NO reduction from flue gases *J. Appl. Phys.* **82** 4781–94
[65] Keppens R, Teunissen J, Xia C and Porth O 2021 MPI-AMRVAC: a parallel, grid-adaptive PDE toolkit *Comput. Math. Appl.* **81** 316–33

[66] Mott-Smith B H M and Langmuir I 1926 The theory of collectors in gaseous discharge *Phys. Rev.* **28** 727
[67] Xue M, Peng S, Wang F, Ou J, Li C and Li W 2017 Linear relation between surface roughness and work function of light alloys *J. Alloys Compd.* **692** 903–7
[68] Li W and Li D Y 2005 On the correlation between surface roughness and work function in copper *J. Chem. Phys.* **122** 064708
[69] Freiburg A, Jäger W and Flügge J 1991 Investigation of oxide films on ferritic stainless steel *Fresenius J. Anal. Chem.* **341** 427–31
[70] Mignolet J C P *et al* 1963 Nature of thin oxide films on metals as revealed by work function measurements *Nature* **200** 648–9
[71] Uhrlandt D, Baeva M, Pipa A V, Kozakov R and Gött G 2015 Cathode fall voltage of tig arcs from a non-equilibrium arc model *Weld. World* **59** 127–35
[72] Oliveira C, Reis J L, Souza-Corrêa J A, Dal Pino A and Amorim J 2012 Optical and electrical diagnostics of a spark-plug discharge in air *J. Phys. D: Appl. Phys.* **45** 255201
[73] Staack D, Farouk B, Gutsol A and Fridman A 2008 DC normal glow discharges in atmospheric pressure atomic and molecular gases *Plasma Sources Sci. Technol.* **17** 25013
[74] Staack D, Farouk B, Gutsol A F and Fridman A A 2006 Spectroscopic studies and rotational and vibrational temperature measurements of atmospheric pressure normal glow plasma discharges in air *Plasma Sources Sci. Technol.* **15** 818–27
[75] Huang S, Li T, Zhang Z and Ma P 2019 Rotational and vibrational temperatures in the spark plasma by various discharge energies and strategies *Appl. Energy* **251** 113358
[76] Staack D, Farouk B, Gutsol A F and Fridman A 2007 Spatially resolved temperature measurements of atmospheric-pressure normal glow microplasmas in air *IEEE Trans. Plasma Sci.* **35** 1448–55
[77] Yu L, Laux C O, Packan D M and Kruger C H 2002 Direct-current glow discharges in atmospheric pressure air plasmas *J. Appl. Phys.* **91** 2678
[78] Machala Z, Marode E, Laux C O and Kruger C H 2004 DC glow discharges in atmospheric pressure air *J. Adv. Oxid. Technol.* **7** 133–7
[79] Benilov M S 2008 Bifurcations of current transfer through a collisional sheath with ionization and self-organization on glow cathodes *Phys. Rev.* E **77** 036408
[80] Korolev I D and Mesiats G A 2001 Physics of pulsed breakdown in gases *IEEE Electr. Insul. Mag* **17** 60–61
[81] Nahemow M and Wainfan N 1963 Study of the cathode-fall region in a pulsed glow discharge *J. Appl. Phys.* **34** 2988–92
[82] Kozhevnikov V Y, Kozyrev A V and Korolev Y D 2006 Drift model of the cathode region of a glow discharge *Plasma Phys. Rep.* **32** 949–59
[83] Sukhinin G I and Fedoseev A V 2003 Abnormal and subnormal regimes of a spherical glow discharge in the drift-diffusion approximation *Plasma Phys. Rep.* **29** 1062–9